JCB Journal of Cell Biology

ARTICLE

FAM43A coordinates mtDNA replication and mitochondrial biogenesis in response to mtDNA depletion

Alva G. Sainz[1], Gladys R. Rojas[1], Alexandra G. Moyzis[1], Matthew P. Donnelly[1,2,3], Kailash C. Mangalhara[1], Melissa A. Johnson[1,3], Pau B. Esparza-Moltó[1], Kym J. Grae[1], Reuben J. Shaw[1], and Gerald S. Shadel[1]

Mitochondrial retrograde signaling (MRS) pathways relay the functional status of mitochondria to elicit homeostatic or adaptive changes in nuclear gene expression. Budding yeast have "intergenomic signaling" pathways that sense the amount of mitochondrial DNA (mtDNA) independently of oxidative phosphorylation (OXPHOS), the primary function of genes encoded by mtDNA. However, MRS pathways that sense the amount of mtDNA in mammalian cells remain poorly understood. We found that mtDNA-depleted IMR90 cells can sustain OXPHOS for a significant amount of time, providing a robust model system to interrogate human intergenomic signaling. We identified FAM43A, a largely uncharacterized protein, as a CHK2-dependent early responder to mtDNA depletion. Depletion of FAM43A activates a mitochondrial biogenesis program, resulting in an increase in mitochondrial mass and mtDNA copy number via CHK2-mediated upregulation of the p53R2 form of ribonucleotide reductase. We propose that FAM43A performs a checkpoint-like function to limit mitochondrial biogenesis and turnover under conditions of mtDNA depletion or replication stress.

Introduction

In mammals, mitochondrial DNA (mtDNA) is a maternally inherited, multicopy circular genome that encodes 13 essential proteins of the oxidative phosphorylation (OXPHOS) system, 22 tRNA and 2 rRNA (Shadel and Clayton, 1997). More than 1,200 genes in the nucleus encode the remainder of the mitochondrial proteome, including additional OXPHOS proteins and factors necessary for mtDNA gene expression and replication, highlighting the need for bidirectional communication between mitochondria and the nucleus (Gustafsson et al., 2016). Mitochondrial retrograde signaling (MRS) pathways are a key aspect of this communication (Butow and Avadhani, 2004; Eisenberg-Bord and Schuldiner, 2017; Ryan and Hoogenraad, 2007). Mitochondria signal through a multitude of second messengers, including ROS, metabolites, and even mtDNA itself, to elicit adaptive changes in nuclear gene expression to maintain or change mitochondrial function under physiological, stress, or pathological conditions (e.g., activation of antioxidant responses, modulation of mitochondrial metabolism, and induction of inflammatory signaling) (Martínez-Reyes and Chandel, 2020; Newman and Shadel, 2023; Shadel and Horvath, 2015). Since mutations and depletion of mtDNA cause or are associated with human diseases, elucidating MRS pathways triggered by changes in mtDNA status in humans may help better understand early events in mtDNA disease pathogenesis and identify new therapeutic targets. (Greaves et al., 2012; Suomalainen and Isohanni, 2010; Suomalainen and Nunnari, 2024).

A balance of mitochondrial biogenesis and degradation maintains mitochondrial mass and, in turn, mtDNA copy number under homeostatic conditions. PGC-1α is a primary regulator of mitochondrial biogenesis in many cells, coordinating the expression of genes in the nucleus encoding mitochondrial proteins, including transcription factor A, mitochondrial (TFAM). TFAM is an abundant mtDNA-binding protein that regulates transcription, transcription-dependent mtDNA replication, and mtDNA organization. In addition to TFAM, replication of mtDNA is dependent on the nucleus-encoded DNA replisome (DNA polymerase gamma, POLG, and other factors) and a steady supply of deoxynucleotides provided by nucleotide salvage pathways or de novo synthesis by ribonucleotide reductase (RNR). Two forms of RNR catalyze the conversion of ribonucleotides to deoxynucleotides for use in mtDNA and nuclear DNA repair and replication. A homodimer of the larger alpha subunit (RRM1), which is common to both forms, associates with a homodimer of one of two smaller homologous beta subunits

---

[1]The Salk Institute for Biological Studies, La Jolla, CA, USA; [2]Medical Scientist Training Program, University of California, San Diego, La Jolla, CA, USA; [3]Biomedical Sciences Graduate Program, University of California, San Diego, La Jolla, CA, USA.

Correspondence to Gerald S. Shadel: gshadel@salk.edu.

https://doi.org/10.1083/jcb.202311082

(RRM2 or p53R2) (Aye et al., 2015). Checkpoint kinase 2 (CHK2) is a serine–threonine kinase that regulates the nuclear DNA damage response. For example, in response to nuclear DNA double-strand breaks, Ataxia-Telangiectasia mutated (ATM) kinase phosphorylates CHK2, which then amplifies this response by phosphorylating myriad downstream effector proteins involved in DNA repair, cell cycle arrest, nucleotide biosynthesis, and apoptosis (Chen et al., 2005; Eaton et al., 2007; Matsuoka et al., 2000). However, CHK2 is also activated in response to mitochondrial signals, including ROS and mtDNA damage or depletion (Crider et al., 2012; Koczor et al., 2009; Schroeder and Shadel, 2014). We and others have shown that activation of CHK2 leads to an increase in mtDNA abundance mediated through the upregulation of RNR (Lebedeva and Shadel, 2007; Niu et al., 2012; Taylor et al., 2005). Mutations in RRM1 and p53R2 cause mtDNA depletion syndromes (MDS) in humans, highlighting the importance of the p53R2-containing form of RNR in maintaining mtDNA (Shintaku et al., 2022; Suomalainen and Isohanni, 2010). The failure to coordinate mitochondrial biogenesis, mtDNA replication, and nucleotide availability can render the cell unable to properly respond to mitochondrial stress (i.e., ETC disruptions, mtDNA damage/depletion) or changes in energetic demand, promoting cellular dysfunction and disease (Ploumi et al., 2017).

Prior work in budding yeast (*S. cerevisiae*) revealed the existence of MRS networks that respond specifically to the amount or structure of mtDNA (Parikh et al., 1987; Woo et al., 2009). Through comparative gene expression analysis of yeast strains with (*rho*$^+$) or without (*rho*^{o}) mtDNA or that lack OXPHOS activity but retain mtDNA, Woo et al. (Woo et al., 2009) defined "intergenomic signaling" as a specific MRS pathway that communicates the presence or absence of mtDNA independently of OXPHOS capacity. The nature of intergenomic signaling in mammals is less well understood. Most previous studies investigating the mammalian MRS responses to mtDNA depletion were conducted in cancer cells, which have altered mitochondria and metabolic pathways, or in primary cells where mtDNA was stably depleted or absent (Crider et al., 2012; Dagsgaard et al., 2001; Eisenberg-Bord and Schuldiner, 2017; Schroeder and Shadel, 2014; West et al., 2015; Woo et al., 2009; Wu et al., 2019). These approaches prevent interrogation of the early stages of intergenomic signaling triggered by mtDNA depletion since they reduce OXPHOS capacity and activate energetic stress pathways. Thus, in this study, we used a primary human cell model of acute mtDNA depletion in which OXPHOS activity is maintained to investigate human intergenomic signaling. This strategy uncovered FAM43A as an early responder to mtDNA depletion that serves an mtDNA checkpoint-like function in collaboration with the stress kinase CHK2.

Results

A human cell model of intergenomic signaling

Treatment of IMR90 primary human fetal lung fibroblasts with 2′3′-dideoxycytidine (ddC), a chain-terminating deoxynucleoside analog that selectively inhibits mtDNA replication by DNA polymerase gamma (POLG) (Chen and Cheng, 1989), resulted in a gradual loss of mtDNA, with ~95% mtDNA depletion at 96 h (Fig. 1 A). Removal of the drug allowed the eventual recovery of mtDNA copy number, showing that mtDNA depletion via this method is reversible (Fig. S1 A). As expected, mtDNA depletion was accompanied by reduced steady-state abundance of TFAM, an abundant mtDNA-binding protein and transcription factor, the level of which usually mirrors the copy number of mtDNA (Fig. S1 B) (Larsson et al., 1998). The absence of or prolonged partial depletion of mtDNA has been reported to induce cell cycle arrest and cellular senescence in yeast and mammalian systems (Wiley et al., 2016; Crider et al., 2012; Park et al., 2004). To assess whether acute mtDNA depletion impairs proliferation in IMR90 cells, we measured the incorporation of 5-ethynyl-2′deoxyuridine (EdU) into nuclear DNA, which reflects progression through the S-phase. IMR90 cells acutely depleted of mtDNA showed comparable levels of nuclear EdU incorporation to untreated (UNT) controls (Fig. 1 B). Depleting mtDNA also did not affect the long-term proliferative potential of IMR90 cells or alter the expression of p16, an inhibitor of cell cycle progression and a common marker of cellular senescence (Fig. S1, B and C).

Next, we tested whether mtDNA-depleted IMR90 cells displayed changes in mitochondrial abundance or OXPHOS function. Acute depletion of mtDNA did not affect mitochondrial mass, membrane potential, or the total cellular levels of ATP or hydrogen peroxide (H_2O_2) (Fig. 1, C–F). Seahorse metabolic flux analysis revealed that mtDNA-depleted IMR90 cells have similar oxygen consumption profiles to control (UNT) cells (Fig. 1 G). Neither basal oxygen consumption rate (OCR) nor spare respiratory capacity was significantly altered by mtDNA depletion (Fig. 1, H and I). Interestingly, 96 h of ddC treatment resulted in a loss of ~95% of mtDNA but only minimally affected the steady-state abundance of core OXPHOS subunits (Fig. S1, D and E), indicating fairly robust stability of the OXPHOS complexes in these cells under these conditions. Previous studies have shown that the rate of mitochondrial respiration and ATP synthesis is only affected once the activity or expression of OXPHOS components decreases below a certain threshold, a phenomenon termed the "biochemical threshold effect" (Rossignol et al., 2003; Spelbrink et al., 1994). The ability of IMR90 cells to maintain OXPHOS complexes above this threshold while mtDNA is severely depleted should prevent the activation of energy-sensitive MRS pathways, making IMR90 cells a useful human cell model in which to interrogate intergenomic signaling.

FAM43A is an early responder to mtDNA depletion

Having established this IMR90 cell model of intergenomic signaling, we performed RNA sequencing in cells treated with vehicle or ddC for 24, 48, 72, and 96 h to identify factors involved in the acute response to mtDNA depletion (Table S1). Differential gene expression analysis revealed minimal changes during the first 3 days of treatment, consistent with the lack of mitochondrial dysfunction or energetic/proliferative defects. No significant ($P < 0.05$, $\log_2$ fold change >0.58 and less than −0.58) differentially expressed genes (DEGs) were detected after 24 h of treatment, two DEGs were detected after 48 h (*FAM43A* and *GDF15*), and seven DEGs were detected after 72 h (*ACTA2*, *GDF15*, *MAMDC2*, *RDH10*, *CDKN1A*, *FAM43A*, *FDXR*) (Table S2). All

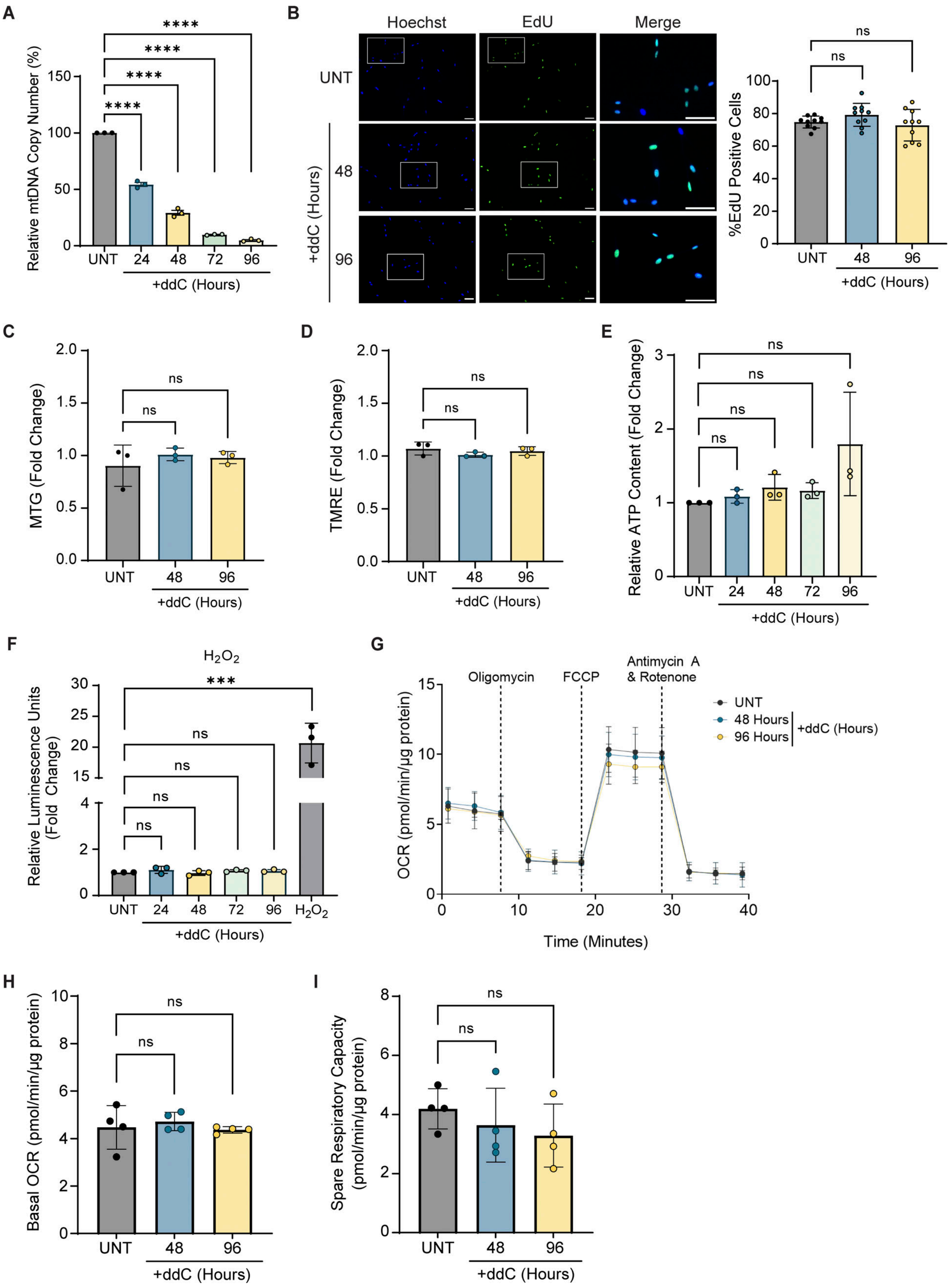

Figure 1. **Depletion of mtDNA in IMR90 cells as a model of intergenomic signaling. (A)** Relative mtDNA copy number of cells treated with ddC (20 µM) for the indicated time measured by qPCR with ND1 primers, normalized to nuclear B2M. The relative mtDNA copy number of untreated (UNT) cells was given a value of 100%. Data points represent the mean of three technical replicates from three biological replicates. Error bars represent mean ± SD, one-way ANOVA

with Dunnett's multiple comparisons; ****, P < 0.0001. **(B)** Representative fluorescent images and quantification of control UNT cells and cells treated with ddC for the indicated times showing colocalization of EdU (green) and Hoechst-stained (blue) nuclei (*n* = 10 from two biological replicates). Scale bar: 100 µm. Error bars represent mean ± SD. One-way ANOVA with Dunnett's multiple comparisons; ns, P > 0.05. **(C and D)** Mitochondrial mass and (D) membrane potential of control UNT cells and cells treated with ddC for the indicated time. Data points represent the mean of three technical replicates from three biological replicates. Error bars represent mean ± SD, multiple Unpaired Student's *t* test; ns, P > 0.05. **(E and F)** ATP and (F) hydrogen peroxide (H_2O_2) measurements of control UNT cells and cells treated with ddC for the indicated time. Data points represent the mean of three technical replicates from three biological replicates. Error bars represent mean ± SD, multiple Unpaired Student's *t* test; ns, P > 0.05. **(G)** Oxygen consumption rate during Seahorse metabolic flux assay of untreated and cells treated with ddC for the indicated time (*n* = 4 biological replicates). Error bars represent mean ± SD. **(H and I)** Basal oxygen consumption and (I) Spare respiratory capacity (from G) of control UNT cells and cells treated with ddC for the indicated time (*n* = 4 biological replicates). Error bars represent mean ± SD, multiple Unpaired Student's *t* test; ns, P > 0.05.

significant DEGs detected at 48 and 72 h remained altered at 96 h, indicating that an initial gene program is activated when mtDNA is depleted below 50% that persists and expands as mtDNA depletion becomes more severe (Fig. 2 A). Due to the small number of DEGs at all time points, pathway analysis was largely uninformative. However, gene set enrichment analysis of transcription factor networks revealed that the E2F transcription factor network was downregulated in cells treated with ddC for 96 h (Fig. S1 F and Table S3). E2F transcription factors play critical roles in regulating the timely expression of genes required for entry and progression through the S-phase (Sheldon, 2017). Although a proliferative defect was not observed in mtDNA-depleted IMR90 cells, the downregulation of E2F signaling may indicate that cells are beginning to activate other stress responses after 96 h of mtDNA depletion. Therefore, we decided to focus on gene expression changes identified at earlier stages of mtDNA depletion.

Expression of *FAM43A* and *GDF15* was upregulated at 48 h of ddC treatment, and this persisted through 96 h of treatment, suggesting that these factors may be key mediators of intergenomic signaling. Notably, GDF15 is often elevated in patients harboring single or multiple mtDNA deletions and defects in mitochondrial translation, but not usually in patients with defects in OXPHOS complexes (Formichi et al., 2020). Thus, GDF15 may be upregulated primarily by changes in mtDNA status independently of OXPHOS function under certain conditions, supporting our models' utility for identifying factors potentially involved in intergenomic signaling. Since the expression profile of *FAM43A* was similar to *GDF15* (Fig. 2 B), we hypothesized that FAM43A may be a novel player in intergenomic signaling. FAM43A is a largely uncharacterized protein identified as a biomarker associated with membranous nephropathy and a prognostic marker for the recurrence of triple-negative breast cancer (Chen et al., 2011; Zhou et al., 2021). The *FAM43A* transcript is also highly upregulated in neuroendocrine cell lines that display increased sensitivity to mitochondrial electron transport chain inhibitors and oxidative stress-induced cell death (Chandiramani et al., 2011). Although these studies identified interesting associations between FAM43A expression and disease phenotypes, the function of FAM43A was not investigated.

RT-qPCR analysis confirmed that 48 h of ddC treatment upregulated the expression of *FAM43A* in IMR90 cells (Fig. 2 C). Upregulation of *FAM43A* was also observed in IMR90 cells treated with ethidium bromide (EtBr) and in liver tissue from inducible heterozygous $Tfam^{+/-}$ mice, supporting that FAM43A is transcriptionally upregulated by mtDNA depletion in both human and mouse and this is not an off-target effect of ddC (Fig. S1, G–I). We next investigated the localization and abundance of FAM43A protein under basal and mtDNA-depleted conditions by fluorescence microscopy. FAM43A forms small punctate cytoplasmic structures in untreated cells, showing little to no colocalization with markers of various organelles, including mitochondria, nuclei, and autophagosomes (Fig. S2). The expected colocalization between replicating mtDNA nucleoids and mitochondria (HSP60) was measured as a positive control (Fig. S2 B). Depletion of mtDNA increased FAM43A protein levels and dramatically changed FAM43A morphology (Fig. 2 D and Fig. S2). Treatment with ddC for 96 h led to the formation of cytoplasmic FAM43A aggregates (Fig. 2 D and Fig. S2). These aggregates do not show a strong colocalization with any of the assessed organelles, and ddC treatment does not significantly alter the colocalization of FAM43A and organelle markers compared with untreated control cells (Fig. S2). FAM43A protein levels remained high 96 h after the removal of ddC, but returned to control (UNT) levels after 192 h (Fig. 2, D and E). In contrast, the number of FAM43A aggregates significantly decreased after 96 h of mtDNA recovery and returned to UNT levels after 192 h (Fig. 2, D and F). Additional quantification of this was not possible because the available FAM43A antibodies do not work for immunoblotting. These data suggest that aggregate formation is not simply the result of increased FAM43A protein and is more likely due to a signaling event triggered by mtDNA depletion that terminates when mtDNA is repleted.

Knockdown of FAM43A activates mitochondrial biogenesis and turnover

To begin to elucidate the function of FAM43A, we reduced its expression using siRNA. Depletion of *FAM43A* in IMR90 cells increased mitochondrial mass with no change in mitochondrial membrane potential when normalized to mitochondrial abundance (Fig. 3, A–D). Depletion of *FAM43A* also increased mtDNA copy number in IMR90 cells and mouse embryonic fibroblasts (MEFs), demonstrating that FAM43A likely has a conserved role in regulating mitochondrial and mtDNA abundance in mammals (Fig. 3, E–G). The increase in mtDNA copy number was also observed in *FAM43A*-knockout (FKO) H292 (human lung mucoepidermoid carcinoma) cells, validating the knockdown approach (Fig. S3, A and B). An increase in mitochondrial mass and mtDNA copy number can be caused by a decrease in mitochondrial turnover and/or an increase in mitochondrial biogenesis and mtDNA replication. To address the possibility of changes in mitochondrial turnover, we measured autophagy/

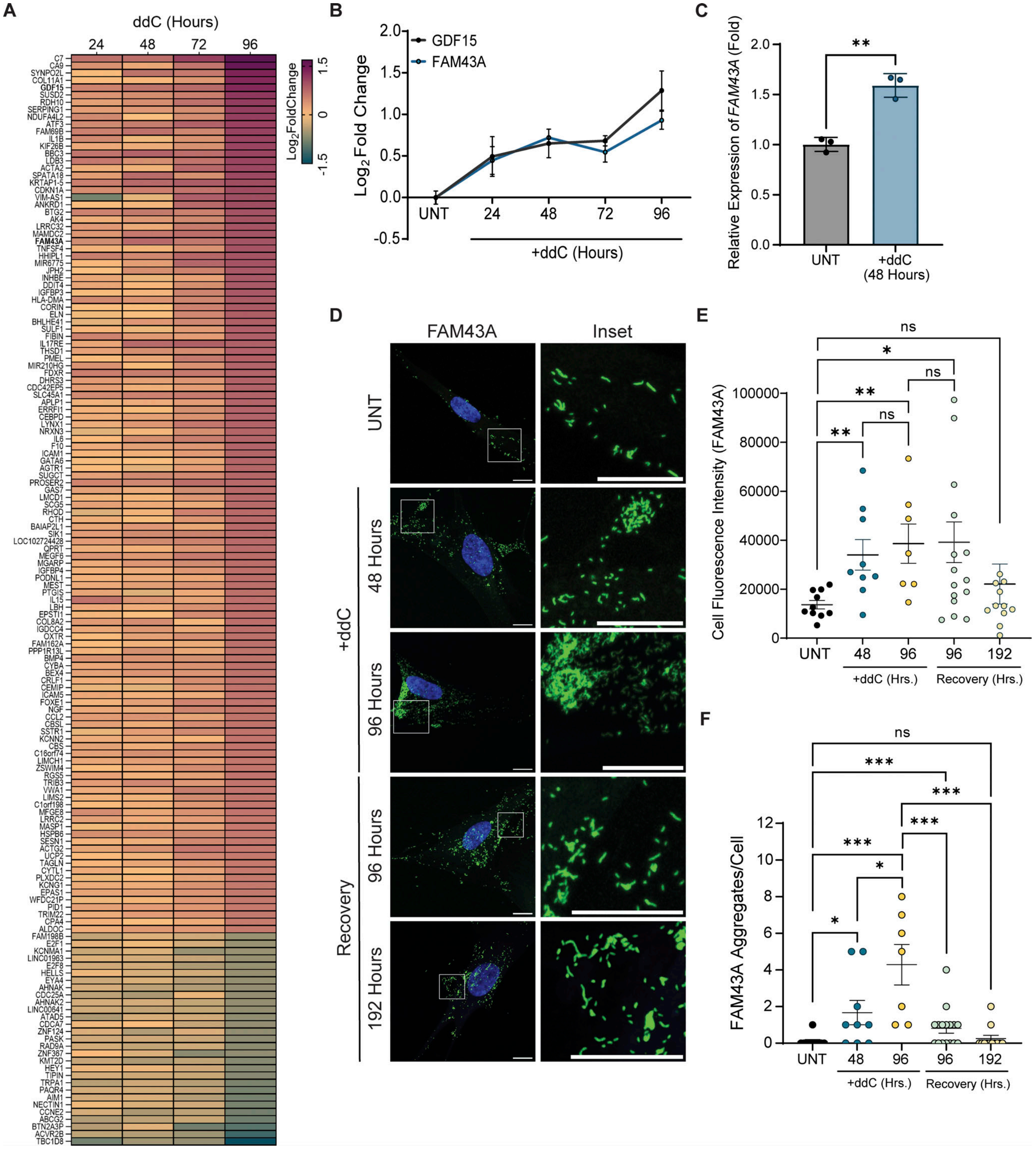

Figure 2. **FAM43A is an early responder to mtDNA depletion. (A)** Heatmap representing the mean $\log_2$ fold-change values of differentially expressed genes in IMR90 cells treated with ddC (20 µM) for the indicated time (*n* = 2–3 biological replicates per condition) relative to untreated (UNT) control cells. The heatmap shows the expression of the 151 significantly up- and downregulated genes identified in IMR90 cells treated with ddC for 96 h and their expression across all time points. **(B)** Log_2 fold-change values of *GDF15* and *FAM43A* between UNT and IMR90 cells treated with ddC for the indicated times. Data points represent the mean $\log_2$ fold-change from three biological replicates. Error bars represent mean ± SD. **(C)** Relative *FAM43A* mRNA levels in IMR90 cells treated with ddC for 48 h relative to UNT control cells measured by RT-qPCR normalized to *ACTIN* (*n* = 3 technical triplicates). Error bars represent mean ± SD, Unpaired Student's *t* test; *, $P < 0.05$. **(D)** Representative Airyscan images of endogenous FAM43A (green) and nuclei (blue) in UNT cells (top), cells treated with ddC (+ddC) for 48 or 96 h, and cells 96 and 192 h after removal of ddC (Recovery). Insets show the morphological change of FAM43A during mtDNA depletion and repletion. Scale bar: 10 µm. **(E and F)** Quantification of the fluorescence intensity of FAM43A signal and (F) number of FAM43A aggregates per cell in UNT (*n* = 10 from two biological replicates). ddC-treated (48 h [*n* = 9 from two biological replicates] and 96 h [*n* = 7 from two biological replicates]), and cells 96 (*n* = 15 from two biological replicates) and 192 h (*n* = 11 from two biological replicates) after removal of ddC. Error bars represent mean ± SEM, multiple unpaired Student's *t* test; ns, $P > 0.05$; *, $P < 0.05$; **, $P < 0.01$; ***, $P < 0.001$.

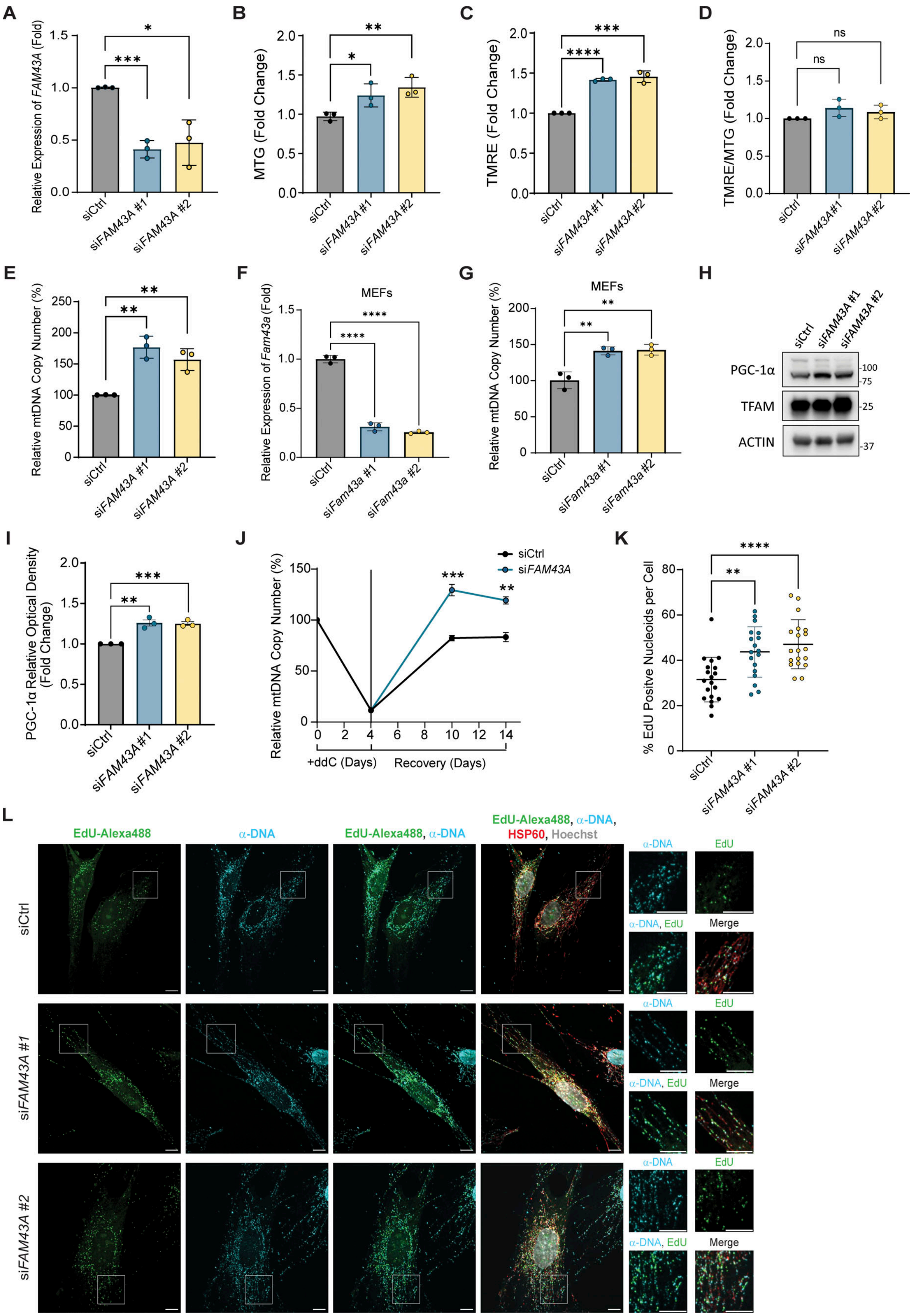

Figure 3. **FAM43A inhibits mitochondrial biogenesis and mtDNA replication. (A)** Relative *FAM43A* mRNA level in IMR90 cells transfected with the indicated siRNA and collected 96 h after transfection. Expression was measured by RT-qPCR and normalized to *ACTIN*. Data points represent the average of three

biological replicates. Error bars represent mean ± SD, multiple Unpaired Student's *t* test; *, $P < 0.05$: ***, $P < 0.001$. **(B–D)** (B) Mitochondrial mass (Mitotracker Green staining, MTG), (C) Mitochondrial membrane potential (TMRE staining) and (D) MTG/TRME ratio of IMR90 cells measured 96 h after transfection with the indicated siRNA. Data points represent the mean of three technical replicates from three biological replicates and normalized to the value of the control siRNA (siCtrl), which was given a value of 1.0. Error bars represent mean ± SD, multiple unpaired Student's *t* test; *, $P < 0.05$; **, $P < 0.01$; ***, $P < 0.001$; ****, $P < 0.0001$. **(E)** Relative mtDNA copy number of IMR90 cells transfected with the indicated siRNA and collected 96 h after transfection measured by qPCR with ND1 primers, normalized to nuclear B2M. Data points represent the mean of three technical replicates from three biological replicates. Error bars represent mean ± SD, multiple Unpaired Student's *t* test; **, $P < 0.01$. **(F)** Relative *Fam43a* mRNA level of mouse embryonic fibroblasts (MEFs) transfected with the indicated siRNA and collected 96 h after transfection. Expression was measured by RT-qPCR and normalized to *ACTIN* ($n = 3$ technical replicates). Error bars represent mean ± SD, one-way ANOVA with Dunnett's multiple comparisons; ****, $P < 0.0001$. **(G)** mtDNA copy number of MEFs transfected with the indicated siRNA. Expression was measured by qPCR ($n = 3$ technical replicates) using ND1 primers normalized to nuclear Tert. Error bars represent mean ± SD, one-way ANOVA with Dunnett's multiple comparisons; **, $P < 0.01$. **(H)** Representative immunoblots of PGC-1α, TFAM, and ACTIN (loading control) of IMR90 cells transfected with the indicated siRNA for 96 h. **(I)** Quantification of the relative optical density of PGC-1α from three independent experiments treated as in H. Error bars represent mean ± SD, multiple Unpaired Student's *t* test; **, $P < 0.01$. ***, $P < 0.001$. **(J)** IMR90 cells were treated with ddC for 96 h and then transfected with the indicated siRNA (si*FAM43A* #1). Samples were collected at the end of ddC treatment (first two points) and 10- and 14-days after transfection. Data points represent the mean of three technical replicates from three biological replicates. Error bars represent mean and error ± SD, multiple unpaired Student's *t* test; **, $P < 0.01$; ***. $P < 0.001$. **(K)** Quantification of Pulse EdU labeling (4 h) in IMR90 cells at 96 h after transfection with control ($n = 18$ from two biological replicates) or FAM43A siRNAs ($n = 18–19$ from two biological replicates). Error bars represent mean ± SD, one-way ANOVA with Dunnett's multiple comparisons; **, $P < 0.01$; ****. $P < 0.0001$. **(L)** Representative spinning disk images of Alexa488-EdU (green), DNA (blue), HSP60 (red), and Hoechst (gray). Insets show the colocalization between EdU and DNA (bottom left) and the merge of all signals (bottom right). Scale bar: 10 µm. Source data are available for this figure: SourceData F3.

mitophagy induction. Treatment of *FAM43A*-knockdown cells with chloroquine (CQ), an inhibitor of autophagosome–lysosome fusion, resulted in an accumulation of LC3-II that exceeded the accumulation observed in CQ-treated control cells, indicating that autophagic activity is higher in *FAM43A*-depleted cells (Fig. S3, C and D) (Bensalem et al., 2021; Klionsky et al., 2016; Mauthe et al., 2018). Interestingly, the depletion of mtDNA decreased autophagic activity in IMR90 cells, demonstrated by a reduction in the accumulation of LC3-II after CQ treatment compared with untreated cells (Fig. S3, E and F). Since mtDNA depletion increases FAM43A expression, we hypothesized that FAM43A might contribute to the decrease in autophagic activity observed in mtDNA-depleted cells. Consistent with this, the depletion of *FAM43A* partially restored autophagic activity in mtDNA-depleted cells (Fig. S3, G and H).

Next, we measured mitophagy specifically using IMR90 cells stably expressing mitochondrial mKeima and found that, despite the increase in mitochondrial mass observed in *FAM43A*-knockdown cells, there was an increase in mitophagy flux (Fig. S3 I). The increase in mitochondrial turnover was accompanied by an increase in PGC-1α, a key regulator of mitochondrial biogenesis, suggesting that the increase in mitochondrial mass in *FAM43A*-knockdown cells was driven by an increase in mitochondrial biogenesis that outpaced mitochondrial turnover (Fig. 3, H and I). A key step in generating more mitochondria is increasing mtDNA copy number to support the production of OXPHOS complexes. To measure mtDNA replication in *FAM43A*-knockdown cells, we performed mtDNA depletion–repletion experiments (Fig. 3 J). Following 96 h of ddC treatment, cells were transfected with control or siRNA against *FAM43A* and cultured in a ddC-free medium. After 14 days of recovery, *FAM43A*-knockdown cells recovered ∼120% of the original mtDNA copy number of parental IMR90 cells (i.e., had more mtDNA than they started with), whereas control cells (with FAM43A) had repleted only ∼83% of their mtDNA (Fig. 3 J). Additionally, the rate of EdU incorporation into mtDNA nucleoids (% EdU positive nucleoids per cell) was significantly higher in *FAM43A*-knockdown cells (Fig. 3, K and L), indicating an increase in mtDNA replication. These data indicate that the increase in mitochondrial mass and mtDNA copy number in *FAM43A*-knockdown cells is driven by an increase in mitochondrial biogenesis that overcomes the increase in mitophagy.

In addition to maintaining cellular quality control, autophagy also salvages biosynthetic building blocks, including nucleotides and amino acids (Aman et al., 2021). In budding yeast, loss of autophagy impairs mtDNA synthesis during starvation by decreasing dNTP pools, underscoring the role of autophagy in providing the mitochondria with deoxynucleotides during stress (Medeiros et al., 2018). Additionally, the deletion of *ATG7* in KRAS-driven lung tumors results in a significant drop in nucleoside phosphates and mitochondrial dysfunction, which can be rescued by exogenous nucleoside supplementation (Guo et al., 2016). Therefore, we reasoned that the increase in autophagy might be supporting mtDNA replication in *FAM43A*-knockdown cells. However, when we knocked down *FAM43A* in IMR90 cells stably expressing shRNA against *ATG5* (Fig. S3 J), mtDNA copy number increased to a similar extent as in control ($ATG5^+$) cells (Fig. S3 K). Knockdown of *FAM43A* also increased mtDNA copy number in *ATG7* knockout H292 cells, further supporting that autophagy is not involved in supporting mtDNA replication in this context (Fig. S3, L and M). Collectively, these data suggest that FAM43A may be a link between mtDNA stress, mitochondrial biogenesis, and mitophagy pathways and serves to restrict mitochondrial biogenesis when mtDNA replication and copy number are low.

FAM43A responds to mtDNA depletion in a CHK2-dependent manner

Previous studies by our group and others identified CHK2 as a key mediator of the cellular response to mtDNA stress. CHK2 is activated by mtDNA damage and depletion and regulates mtDNA copy number by upregulating RNR and increasing dNTP pools (Crider et al., 2012; Niu et al., 2012; Taylor et al., 2005). In IMR90 cells experiencing mtDNA depletion, CHK2 is activated (increase in p^{T68}CHK2/CHK2) in the absence of a transcriptional nuclear

DNA damage response or increases in γH2AX and 53BP1 foci (markers of nuclear DNA damage) (Fig. 4, A–E), implying a noncanonical activation of CHK2 driven by mtDNA depletion. As expected, depletion of mtDNA leads to a CHK2-dependent increase in p53R2, albeit only at the protein level (Fig. 4 F and Fig. S4 A), while *RRM1* transcript levels remained unchanged (Fig. S4 B). The p53R2 subunit of RNR produces the tyrosyl radical required for the catalytic activity of RRM1, driving de novo dNTP synthesis to support mtDNA replication (Guittet et al., 2001; Pontarin et al., 2012). Therefore, acute mtDNA depletion in IMR90 cells activates a previously characterized intergenomic signaling pathway to, presumably, attempt to restore mtDNA copy number by increasing deoxynucleotide availability (Crider et al., 2012; Niu et al., 2012; Taylor et al., 2005). The activation of CHK2 diminishes as cells begin to replete mtDNA, supporting that CHK2 activation is driven by mtDNA levels falling below a certain threshold (Fig. 4, A and B). Interestingly, the kinetics of CHK2 activation and deactivation mirror FAM43A expression and aggregate formation upon mtDNA depletion and repletion (Fig. 4 B and Fig. 2, D–F), suggesting that CHK2 may regulate FAM43A expression or activity in this context. To test this hypothesis, we treated *CHK2*-knockdown cells with ddC for 48 h and examined the expression of *FAM43A*. IMR90 cells with reduced *CHK2* expression failed to upregulate *FAM43A* in response to ddC-mediated mtDNA depletion (Fig. 4 G and Fig. S4 C). Furthermore, treatment of mtDNA-depleted cells with a CHK2 inhibitor (BML-277) prevented the upregulation of *FAM43A*, reduced FAM43A protein and aggregates per cell, demonstrating that mtDNA depletion increases FAM43A expression in a CHK2-dependent manner and that CHK2 kinase activity is necessary to form and maintain FAM43A aggregates (Fig. 4, H–L). These data indicate that CHK2 senses mtDNA depletion in mammals independent of OXPHOS or nuclear DNA damage and upregulates FAM43A protein and aggregate formation as part of an adaptive response to mtDNA stress.

FAM43A knockdown activates CHK2 and RNR-dependent mtDNA synthesis

We next investigated whether *FAM43A* expression had any impact on CHK2 signaling under basal and mtDNA-depleted conditions. Cells depleted of *FAM43A* displayed an increase in CHK2 phosphorylation and CHK2-dependent p53R2 expression, suggesting that FAM43A inhibits CHK2-mediated signaling (Fig. 5, A–C). Activation of CHK2-mediated signaling was confirmed in *FAM43A* knockout (FKO) H292 cells (Fig. S4, D–F). The activation of CHK2 in *FAM43A*-knockdown cells was independent of nuclear DNA damage, similar to what we observed in mtDNA-depleted cells (Fig. S4, G–I). Unlike what we observed during mtDNA depletion, the knockdown of *FAM43A* increased both p53R2 mRNA and protein levels (Fig. 5 C and Fig. S4 J). Interestingly, the activation of CHK2 upon ddC treatment was higher in cells depleted of *FAM43A* compared with mtDNA-depleted control (siCtrl) cells (Fig. 5, D and E). Downstream CHK2 signaling, namely upregulation of p53R2, was also enhanced in *FAM43A*-knockdown cells depleted of mtDNA, suggesting that FAM43A limits CHK2 activation and downstream signaling in the presence of mtDNA stress (Fig. 5 F). Increasing RNR activity is sufficient to increase mtDNA copy number in various model organisms, while prolonged loss of RNR, especially due to reductions in RRM1 and p53R2, causes mtDNA depletion (Fumagalli et al., 2022; Lebedeva and Shadel, 2007; Shintaku et al., 2022). To determine if the increase in p53R2 observed in *FAM43A*-knockdown cells is driving the increase in mtDNA copy number observed under these conditions, we knocked down the expression of p53R2 (RRM2B) or RRM1 in combination with FAM43A. The knockdown of *RRM2B* or *RRM1* abrogated the increase in mtDNA copy number in *FAM43A*-knockdown cells (Fig. 5, G and H; and Fig. S4, K and L), while the knockdown of *RRM2*, the alternative small subunit of RNR, did not (Fig. 5 I and Fig. S4 M). Knockdown of *CHK2* also blunted the increase in mtDNA copy number, consistent with CHK2-mediated upregulation of the p53R2 form of RNR playing a critical role in driving mtDNA synthesis in *FAM43A*-depleted cells (Fig. 5 J and Fig. S4 N).

Discussion

In this study, we developed a human cell culture model of acute mtDNA depletion that enabled us to interrogate the initial stages of intergenomic signaling in the absence of confounding variables like energetic stress and proliferative defects. Using this model, we identified FAM43A, a largely uncharacterized protein in mammals, as an early responder to mtDNA depletion. We found that the knockdown of *FAM43A* activates mitochondrial biogenesis, as evidenced by an increase in mitochondrial mass, mtDNA copy number, and PGC-1α protein. Interestingly, an increase in autophagy and mitochondrial turnover accompanied this biogenesis response. Additionally, we identified a functional connection between CHK2, a known regulator of the cellular response to mtDNA depletion, and FAM43A. Depletion of mtDNA activated CHK2, which, in turn, was necessary for FAM43A upregulation and aggregate formation. Notably, knockdown of *FAM43A* led to basal activation of CHK2 and more robust CHK2 activation (e.g. greater p53R2 upregulation) in response to mtDNA depletion. Thus, we propose FAM43A both suppresses basal CHK2 activation and is part of a negative feedback loop in which CHK2-dependent upregulation of FAM43A ultimately limits maximal CHK2 activity. The upregulation of the CHK2–RNR signaling axis is required for the increase in mtDNA copy number observed in *FAM43A*-knockdown cells, suggesting that CHK2 signaling supports mitochondrial biogenesis by increasing deoxynucleotide availability in cells depleted of *FAM43A*. Collectively, our results support a model in which *FAM43A* is part of an mtDNA depletion checkpoint that coordinates mtDNA replication, deoxynucleotide availability, and mitochondrial biogenesis/turnover via non-canonical CHK2 signaling. We propose that the depletion of mtDNA activates CHK2 to increase RNR activity as a response to replete mtDNA. CHK2 simultaneously activates FAM43A to prevent mitochondrial biogenesis and turnover to maintain mitochondrial mass within a certain threshold until faithful mtDNA replication and mtDNA copy number are restored. In addition, the knockdown of FAM43A induces mitochondrial biogenesis, which involves activating

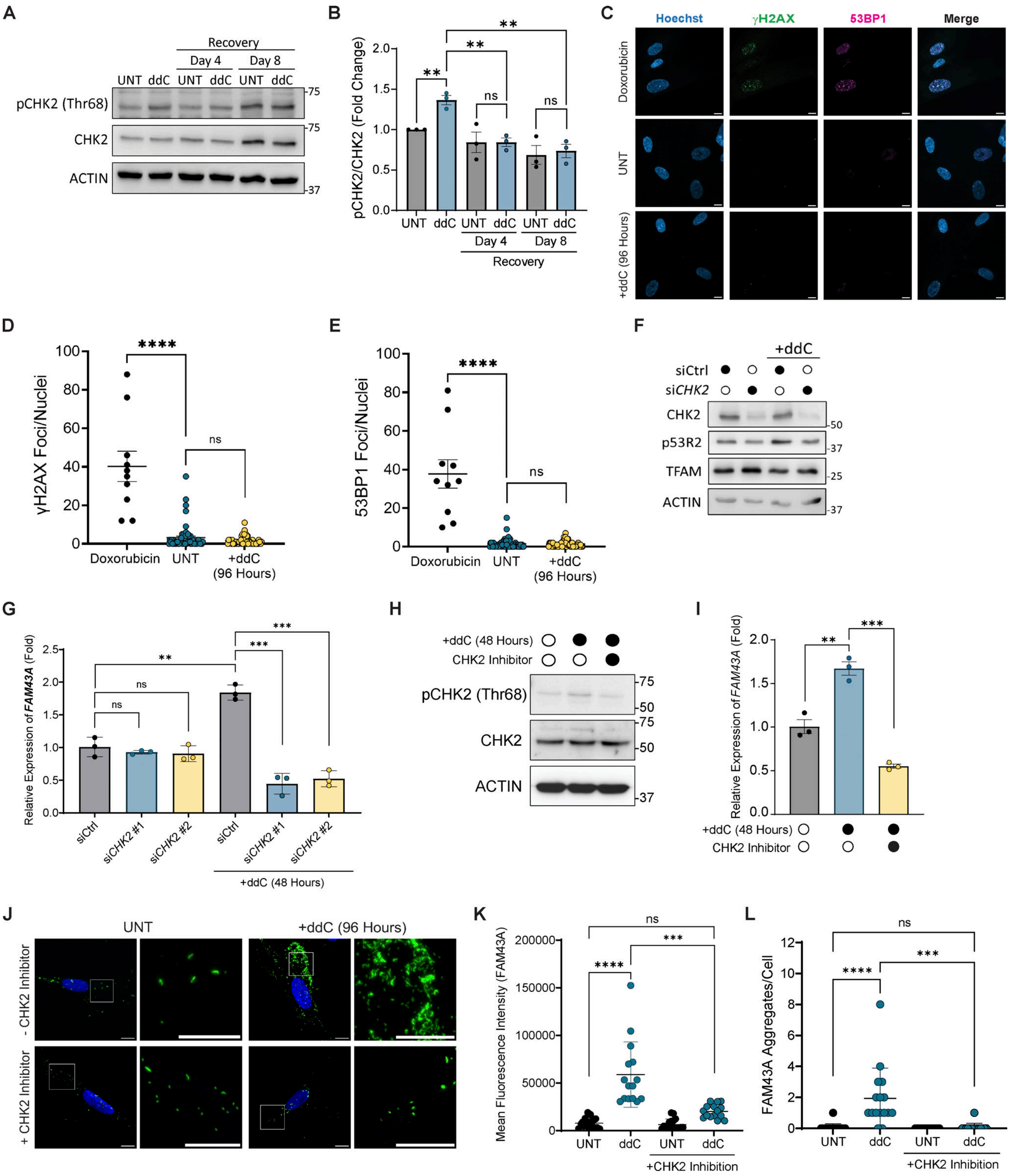

Figure 4. **FAM43A responds to mtDNA depletion in a CHK2-dependent manner. (A)** Representative immunoblots of phosphorylated CHK2 (pCHK2 Thr68), CHK2, and ACTIN (loading control) in untreated (UNT), ddC-treated (96 h), and 4- and 8-days following removal of ddC (Recovery). **(B)** Quantification of (A). The optical density of pCHK2 Thr68 and CHK2 were normalized to loading, and the ratio of pCHK2 Thr68 to total CHK2 was quantified as a measure of CHK2 activation ($n = 3$ biological replicates). Error bars represent mean ± SD, multiple Unpaired Student's *t* test; ns, $P > 0.05$; **, $P < 0.01$. **(C)** Representative spinning disk images of Hoechst (blue), γH2AX (green), and 53BP1 (magenta) in UNT, Doxorubicin-treated (1uM for 4 h), and ddC-treated cells. The merge of these signals is shown in the right column. Scale bar: 10 µm. **(D and E)** Quantification of γH2AX and (E) 53BP1 foci/cell in UNT ($n = 59$ nuclei from two biological replicates), Doxorubicin-treated (1 µM for 4 h) ($n = 10$ nuclei from two biological replicates), and ddC-treated cells ($n = 49$ nuclei from two biological replicates) from (C). Doxorubicin was used as a positive control for nuclear DNA damage. Error bars represent mean ± SEM, multiple Unpaired Student's *t* test; ns, $P > 0.05$; ****, $P > 0.0001$. **(F)** Representative immunoblots of CHK2, p53R2, TFAM, and ACTIN (loading control) of IMR90 cells transfected with the indicated

siRNA. 48 h after transfection, cells were treated with ddC for 48 h and collected for analysis. **(G)** IMR90 cells were transfected with the indicated siRNA. 96 h after transfection, cells were treated with ddC for 48 h. The relative mRNA expression of *FAM43A* was measured by RT-qPCR normalized to *ACTIN* (*n* = 3 technical triplicates). Error bars represent mean ± SD, multiple Unpaired Student's *t* test; ***, P < 0.001; **, P < 0.01; ns, P > 0.05. **(H)** Representative immunoblots of phosphorylated CHK2 (pCHK2 Thr68), CHK2, and ACTIN (loading control) in UNT and cells treated with ddC only or ddC and CHK2 inhibitor (10 µM) for 48 h. **(I)** Relative *FAM43A* mRNA expression in UNT and cells treated with ddC only or ddC and CHK2 inhibitor for 48 h (*n* = 3 technical triplicates). Error bars represent mean ± SD, multiple Unpaired Student's *t* test; **, P < 0.01: ***, P < 0.001. **(J)** Representative Airyscan images of endogenous FAM43A (green) and Nuclei (Hoechst; blue) in UNT and ddC-treated (96 h) IMR90 cells ± CHK2 Inhibitor (48 h). Insets show the morphological change of FAM43A. Scale bar: 10 µm. **(K and L)** Quantification of the fluorescence intensity of FAM43A signal and (L) number of FAM43A aggregates per cell in UNT and cells treated with ddC for 96 h ± CHK2 Inhibitor (*n* = 15 from two biological replicates per condition). Error bars represent mean ± SD, one-way ANOVA with Dunnett's multiple comparisons; ns, P > 0.05; ***, P < 0.001; ****, P < 0.0001. Source data are available for this figure: SourceData F4.

CHK2 to increase mtDNA synthesis via RNR to support the growing mitochondrial network.

The response to acute mtDNA depletion displayed by IMR90 cells allowed us to unmask a novel regulator of the cellular response to mtDNA depletion. IMR90 cells maintained mitochondrial respiration and mitochondrial mass despite severe depletion of mtDNA. Although mitochondria are highly dynamic organelles that undergo almost constant remodeling and turnover, key functional and structural components, such as core OXPHOS subunits, are long-lived in various tissues and can persist for a significant amount of time following transcriptional downregulation, emulating what we observed in IMR90 cells upon mtDNA depletion (Bomba-Warczak et al., 2021; Krishna et al., 2021). It is conceivable that mtDNA depletion may lead to an adaptive stabilization of OXPHOS proteins to maintain mitochondrial OXPHOS as cells attempt to restore normal mtDNA copy number. It is also possible that the stability of mitochondrial mRNAs is increased upon mtDNA depletion to maintain translation of mtDNA-encoded OXPHOS subunits and sustain assembly of the OXPHOS complexes. Notably, we found that the knockdown of *FAM43A* in mtDNA-depleted cells rescued the decrease in autophagy induced by ddC treatment. Further mechanistic studies are required to determine whether the regulation of autophagy by FAM43A is through direct or indirect mechanisms. However, previous studies have shown that the activation of mitochondrial biogenesis is linked to autophagy and mitophagy induction. In addition to driving mitochondrial biogenesis, activation of PGC-1α can promote mitophagy by upregulating the mitophagy receptor FUNDC1 in response to cold stress in brown fat tissue and by stabilizing the mitophagy inducer mitostatin (Liu et al., 2021; Neill et al., 2014). Thus, the increase in autophagy and mitophagy in *FAM43A*-knockdown cells may be a secondary effect of an increase in mitochondrial biogenesis. Disruptions in mitochondrial turnover are associated with many human diseases, including diabetes and neurodegeneration, and modulators of mitochondrial biogenesis and mitophagy have shown promise as potential therapeutic targets (Chen et al., 2023; Whitaker et al., 2016). Inhibition of *FAM43A* may also be a therapeutic strategy to stimulate mitochondrial turnover and ameliorate disease phenotypes, but the mechanism by which FAM43A signals to PGC-1α and the long-term effects of PGC-1α hyperactivation must be investigated further. While our results also suggest that inherited loss or alteration of FAM43A function could result in mtDNA-based diseases, the fact that loss of function increases mtDNA copy number might suggest it could be targeted therapeutically specifically in cases of MDS that are not caused by mutations in RNR.

Our data show that CHK2 kinase activity is required for the upregulation of FAM43A in mtDNA-depleted cells. Whether this regulation is via the direct phosphorylation of FAM43A by CHK2 or a secondary downstream mediator of CHK2 signaling is still unknown. Furthermore, although several studies have reported that CHK2 is activated by mtDNA stress, the actual mitochondrial signal that triggers the activation of CHK2 in the absence of oxidative or energetic stress remains elusive (Crider et al., 2012; Schroeder and Shadel, 2014). Double-strand breaks in mtDNA cause altered mitochondrial membrane and cristae ultrastructure, leading to the activation of the integrated stress response mediated by ATAD3, a mitochondrial membrane protein that interacts with mtDNA nucleoids (Fu et al., 2023). Depletion of mtDNA may also lead to changes in mitochondrial inner membrane structure or the altered localization or activity of nucleoid-associated proteins, which may then relay the presence of mtDNA stress to the rest of the cell. Activation of CHK2 signaling was also shown to increase mtDNA copy number and the frequency of the common 4,977-bp mtDNA deletion (Niu et al., 2012). Accumulation of mtDNA deletions is associated with various diseases, including Kearns-Sayre syndrome (Zeviani et al., 1988), Pearson syndrome (McShane et al., 1991), and neurodegeneration (Tresse et al., 2023). This underscores the importance of precise control of mtDNA replication and maintenance pathways. Restraining mtDNA replication in the presence of mtDNA stress via FAM43A-mediated inhibition of CHK2 activation may be a mechanism to prevent further loss of mtDNA integrity. Thus, we propose that FAM43A is part of an important mtDNA checkpoint along with CHK2.

We found that depletion of mtDNA leads to the formation of large FAM43A aggregates in a CHK2-dependent manner. We also found that CHK2 activation is significantly higher in *FAM43A*-knockdown cells depleted of mtDNA compared to mtDNA-depleted control cells, suggesting that FAM43A limits the maximal degree of CHK2 activation in this context. Although the functional significance of FAM43A aggregation remains unknown, this morphological change may facilitate the inhibition of mtDNA stress-induced CHK2 signaling. A comparative analysis of large-scale protein–protein interactions across two human cell lines revealed a potential interaction between FAM43A and subunits of the Ser/Thr phosphatase 2A (PP2A) (Huttlin et al., 2021). Interestingly, PP2A binds CHK2 to keep it

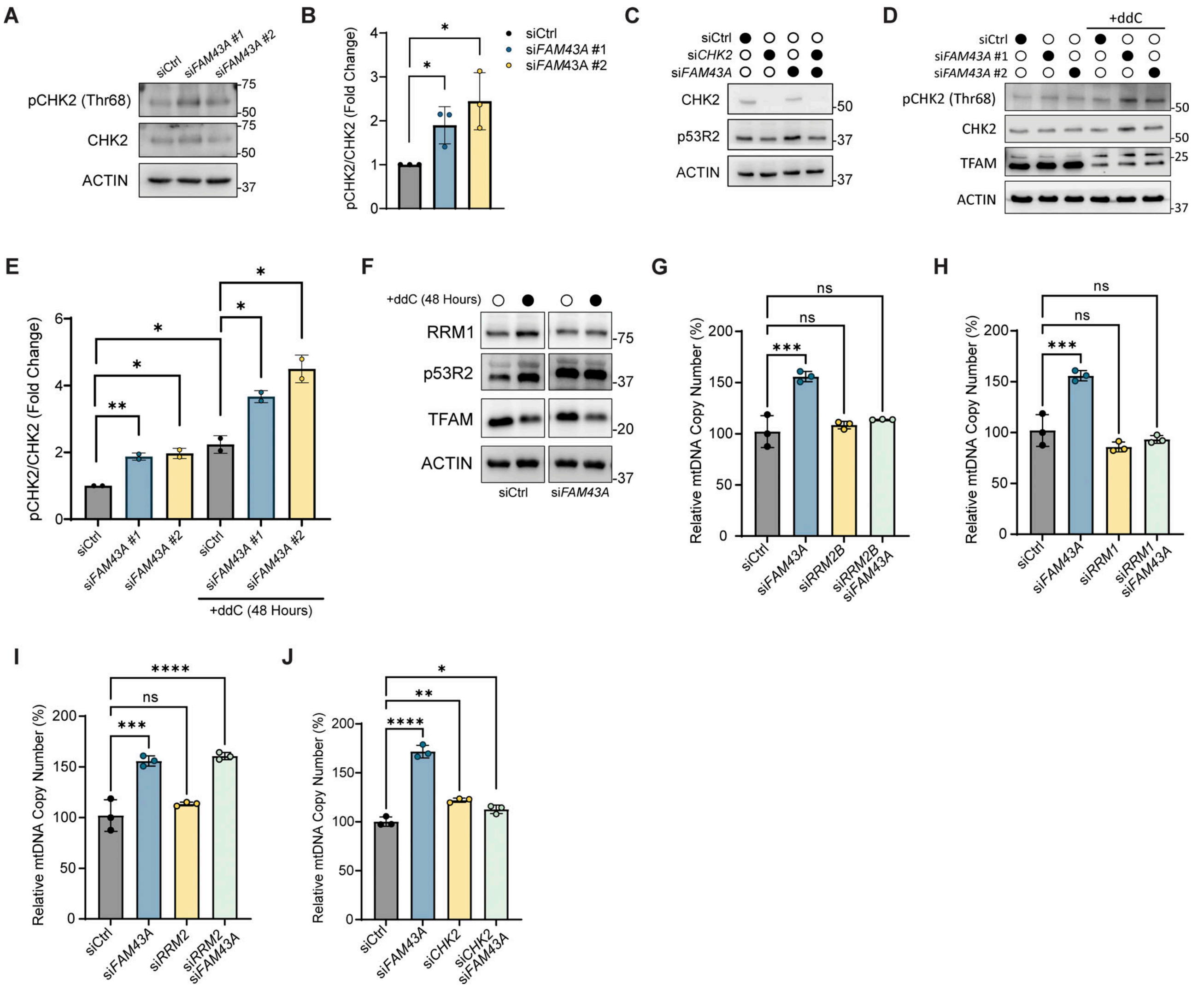

Figure 5. **Knockdown of *FAM43A* activates CHK2 and RNR-dependent mtDNA synthesis. (A)** Representative immunoblots of pCHK2 (Thr68), CHK2, and ACTIN (loading control) in cells transfected with the indicated siRNA and collected 96 h after transfection. **(B)** Quantification of A. The optical density of pCHK2 Thr68 and CHK2 were normalized to loading, and the ratio of pCHK2 Thr68 to total CHK2 was quantified as a measure of CHK2 activation (*n* = 3 biological replicates). Error bars represent mean ± SD, multiple Unpaired Student's *t* test; *, P < 0.05. **(C)** Representative immunoblots of CHK2, p53R2, and ACTIN (loading control) in cells transfected with the indicated siRNA and collected 96 h after transfection. **(D)** Representative immunoblots of pCHK2 Thr68, CHK2, TFAM, and ACTIN (loading control) in cells transfected with the indicated siRNA. 48 h after transfection, cells were treated with ddC and collected 96 h after transfection for analysis. **(E)** Quantification of (D). The optical density of pCHK2 Thr68 and CHK2 were normalized to loading, and the ratio of pCHK2 Thr68 to total CHK2 was quantified as a measure of CHK2 activation (*n* = 2 biological replicates). Error bars represent mean ± SD, multiple Unpaired Student's *t* test; *, P < 0.05; **, P < 0.01. **(F)** Representative immunoblots of RRM1, p53R2, TFAM, and ACTIN (loading control) in cells transfected with the indicated siRNA. After 48 h transfection, cells were treated with ddC and collected 96 h after transfection for analysis. **(G–J)** Relative mtDNA copy number of IMR90 cells transfected with the indicated siRNA and collected for analysis 96 h after transfection as measured by qPCR using ND1 primers, normalized to nuclear B2M. Data points represent the average of technical triplicates from three biological replicates. Data from G–I were normalized to the same control (siCtrl) sample. Error bars represent mean ± SD, one-way ANOVA with Dunnett's multiple comparisons; ns, P > 0.05; *, P < 0.05; ***, P < 0.001; ****, P < 0.0001. Source data are available for this figure: SourceData F5.

inactive under normal conditions and dampens CHK2 activity following the resolution of DNA damage (Freeman et al., 2010). FAM43A possesses a highly conserved phosphotyrosine-independent Dab-like phosphotyrosine binding (PIDPB) domain (Kumar et al., 2022). PIDPB domains often serve as adaptors or scaffolds for organizing signaling complexes (Uhlik et al., 2005). PP2A has been shown to bind to the phosphotyrosine domain of Shc to inhibit Ras/MAP kinase downstream signaling in Rat-1 fibroblasts (Ugi et al., 2002). Thus, we speculate that FAM43A may limit CHK2 phosphorylation through an mtDNA-stress-induced interaction with PP2A. In summary, this study is the first to functionally characterize FAM43A and identify its mtDNA checkpoint-like function. Further interrogation of FAM43A in other cellular contexts, including when CHK2 is activated by other signals, is warranted to fully understand its multifaceted functions in mitochondrial and cellular homeostasis and its potential involvement in human disease.

Materials and methods

Mouse strains and methods

C57BL/6J mice were purchased from The Jackson Laboratory (Strain #: 000664, RRID: IMSR_JAX:000664). Floxed *TFAM* (*Tfam*$^{fl/fl}$) mice (B6.Cg-*Tfam*$^{tm1.1Ncdl}$/J, The Jackson Laboratory, Strain #026123, RRID: IMSR_JAX:026123) were used for the conditional depletion of TFAM in the liver. Heterozygous *Tfam*$^{fl/+}$mice were obtained by breeding homozygous *Tfam*$^{fl/fl}$ floxed with C57BL/6J mice. Wild-type and *Tfam*^{fl} alleles were detected by PCR using primers 5′-GCTGCTTTACCTTCTCAGTGAC-3′and 5′-CAACTTGTGTTGCACACTCC-3′ (for wild-type), and 5′-CTCCTCCAGTGTCGGTCATTG-3′ and 5′-GTCGACGGCGCGTTAATTAATAA-3′ (for *Tfam*^{fl}). At 3 to 4 mo of age, mice were retro-orbitally injected with 1.0 × 10^{11} viral genomes of AAV8-TBG-Cre (#107787; Addgene), which was packaged at the Salk GT3 Core. C57BL/6J mice were used as controls, and both males and females were injected for each genotype. At 4 wk post-injection, mice were humanely euthanized, perfused with PBS through the portal vein, and liver samples were collected. Flash-frozen liver tissue samples were ground with a mortar and pestle pre-cooled with liquid nitrogen and then processed for RNA extraction using the RNeasy Plus Mini Kit (74136; QIAGEN) following the manufacturer's instructions. All animals were housed at the Salk Animal Resources Department with a 6:00–18:00 h light and 18:00–6:00 h dark cycle, room temperatures from 20°C to 22°C, and a humidity range of 30–70%. All animal and husbandry procedures were IACUC-approved and performed in accordance with guidelines and regulations implemented by the Salk Institute Animal Care and Use Committee.

Cell lines and reagents

IMR90 cells (CCL-186) were obtained from ATCC. Wild type and *ATG7*$^{-/-}$ H292 cells were a gift from Dr. Christina Towers (Towers et al., 2019). MEFs were generated from C57BL/6J mice purchased from The Jackson Laboratory (Strain #: 000664). Lenti-X 293T cells were purchased from Takara Bio (632180). All cells were cultured at 37°C under 5% CO$_2$. IMR90 cells were cultured in EMEM (30-2003; ATCC) containing 10% (vol/vol) fetal bovine serum (FBS) (Gibco). H292 cells were cultured in RPMI 1640 medium (11875093; Thermo Fisher Scientific) containing 10% (vol/vol) FBS. MEFs and Lenti-X 293T were cultured in DMEM (10-013-CV; Corning) containing 10% (vol/vol) FBS. Opti-MEM (31985062) and TrypLE Express Enzyme (12605-010) were obtained from Thermo Fisher Scientific. All experiments were conducted on IMR90 cells with a cumulative population doubling of 12–30, and experiments using MEFs were conducted on cells between passage number 3 and 5. Cells were tested for mycoplasma (MycoAlert Mycoplasma Detection Kit, LT07-318; Lonza) once a month.

Generation of mouse embryonic fibroblasts

WT MEFs were generated from mouse embryos between embryonic days 12.5 and 14.5. The intact uterus was removed from euthanized female mice and rinsed once with 70% ethanol before being transferred into a sterile 10-cm cell culture dish containing 10 ml of cold dissection buffer (PBS + 2 mM glucose + 3% [vol/vol] FBS). Embryos were dissected from each sac and transferred to a well of a 6-well plate containing 1 ml of cold dissection buffer. The heads and livers were removed and the processed embryo was minced with curved tweezers. TrypLE Express (2 ml) was added to the well and a P1000 pipette was used to homogenize the remaining embryo. The homogenized embryos were transferred to a 15-ml conical tube and incubated at 37°C for 5–10 min. The digested embryo homogenate was transferred to a 10-cm dish containing 8 ml of DMEM + 10% (vol/vol) FBS. Following overnight incubation, plates were washed with PBS and 10 ml of fresh medium was added. After 1–2 days, MEFs were passaged or frozen down in freezing media (DMEM + 10% [vol/vol] FBS + 10% [vol/vol] DMSO). MEFs at this stage are considered passage 1.

Cell treatments

The following chemicals were used at the indicated concentrations: 2′-3′ dideoxycytidine (ddC) (20 μM diluted in water; D5782; Sigma-Aldrich), EtBr (50 ng/ml diluted in water; E1510; Sigma-Aldrich), chloroquine (CQ) (50–100 μM diluted in PBS; 14194; Cayman Chemical), and CHK2 inhibitor BML-277 (10 μM diluted in DMSO; 17552; Cayman Chemical). All samples designated as untreated (UNT) were treated with the vehicle used for the accompanying drug treatment for the indicated time.

DsiRNA and DNA plasmids

The following siRNAs were obtained from Integrated DNA Technologies: hs.Ri.FAM43A.13.1 (Sense: 5′-rGrGrGrArCrUrUrGrUrUrGrGrArUrArCrUrCrUrGrGrArGAA-3′; Antisense: 5′-rUrUrCrUrCrCrArGrArGrUrArUrCrCrArArCrArArGrUrCrCrCrCrG-3′), hs.Ri.FAM43A.13.2 (Sense: 5′-rCrArGrUrUrArArArGrArCrArUrCrCrArArUrArUrCrUrUAA-3′; Antisense: 5′-rUrUrArArGrArUrArUrUrGrGrArUrGrUrCrUrUrUrArArCrUrGrUrA-3′), mm.Ri.Fam43a.13.1 (Sense: 5′-rUrUrArCrArGrUrUrArArArGrArArArCrCrUrArArUrArUCT-3′; Antisense: 5′-rArGrArUrArUrUrArGrGrUrUrUrCrUrUrUrArArCrUrGrUrArArArC-3′), mm.Ri.Fam43a.13.2 (Sense: 5′-rArArCrUrGrUrCrArCrArGrCrUrUrArUrUrArGrUrGrArCCT-3′; Antisense: 5′-rArGrGrUrCrArCrUrArArUrArArGrCrUrGrUrGrArCrArGrUrUrGrG-3′), hs.Ri.CHEK2.13.1 (Sense: 5′-rArGrCrUrArArArUrCrArUrCrCrUrUrGrCrArUrCrArUrCAA-3′; Antisense: 5′-rUrUrGrArUrGrArUrGrCrArArGrGrArUrGrArUrUrUrArGrCrUrUrU-3′), hs.Ri.RRM1.13.1 (Sense: 5′-rGrGrCrCrArArGrUrCrArArCrArUrUrGrGrArUrArUrUrGTT-3′; Antisense: 5′-rArArCrArArUrArUrCrCrArArUrGrUrUrGrArCrUrUrGrGrCrCrArC-3′), hs.Ri.RRM2.13.1 (Sense: 5′-rGrUrCrCrArArCrArGrArGrArArUrUrCrUrUrUrUrArCrCTT-3′; Antisense: 5′-rArArGrGrUrArArArArGrArArUrUrCrUrCrUrGrUrUrGrGrArCrUrU-3′), hs.Ri.RRM2B.13.1 (Sense: 5′-rCrUrUrUrCrArArArUrUrCrUrCrArUrCrGrArGrArArUrGTT-3′; Antisense: 5′-rArArCrArUrUrCrUrCrGrArUrGrArGrArArUrUrUrGrArArArGrCrC-3′), and negative control DsiRNA(51-01-14-04) (Sense: 5′-rCrGrUrUrArArUrCrGrCrGrUrArUrArArUrArCrGrCrGrUAT-3′; Antisense: 5′-rArUrArCrGrCrGrUrArUrUrArUrArCrGrCrGrArUrUrArArCrGrArC-3′). The following plasmids were obtained from Addgene: psPAX2 (a gift from Didier Trono, #12260; Addgene, RRID: Addgene_12260), pMD2.G (a gift from

Didier Trono, #12259; Addgene, RRID: Addgene_12259), and pHAGE-mt-mKeima (a gift from Richard Youle, #131626; Addgene, RRID: Addgene_131626). The following plasmids were obtained from MilliporeSigma: Mission pLKO.1-puro Empty Vector Control Plasmid DNA (SHC001), pLKO.1-puro shATG5 (TRCN0000150645), pLKO.1-puro shFAM43A (TRCN0000116225).

Lentivirus generation, cell transduction, and siRNA transfection

Mission pLKO.1-puro empty vector control, shFAM43A, and shATG5 plasmids (2 µg) were cotransfected into Lenti-X-293T cells (632180; Takara Bio) with the lentiviral packaging vectors psPAX2 (1.5 µg) and pMD2.G (0.5 µg) using Lipofectamine 3000 Transfection Reagent (L3000015; Thermo Fisher Scientific) at a ratio of 2:1 (Lipofectamine 3000 [µl]: nucleic acid [µg]). Lentivirus was collected 72 h after transfection. For lentiviral transduction, IMR90 cells were seeded at a density of 1.0×10^6 in 60-mm cell culture dishes. After 24 h, cells were transduced with the indicated lentiviral supernatant. Puromycin (1 µg/ml) (InvivoGen, ant-pr-1) selection was started 48 h after transduction and continued for 5 days before cells were used for experiments. For siRNA transfection, cells were plated to achieve a 50–60% density. The next day, transfection of siRNAs at a final concentration of 50 nM was performed using Lipofectamine RNAiMax (1847641; Invitrogen) according to the manufacturer's instructions. Experiments were performed 4–6 days after transfection.

Cas9/RNP assembly and nucleofection

The single or multi-guide sgRNA/Cas9 ribonucleoprotein (RNP) complex was assembled by combining 6 µl of the target sgRNA mix (Synthego Gene Knockout Kit V2, 30 µM) with 1 µl of SpCas9 (Synthego, 20 µM) and 18 µl of Nucleofector Solution and Supplement (Lonza SF Cell Line 4D-Nucleofector X-Kit, 4.5: 1 ratio of solution to supplement). The mixture was incubated for 10 min at room temperature. Meanwhile, H292 cells were trypsinized, pelleted, and resuspended in PBS at a density of 6,000 cells/µl. The RNP-cell solution was prepared by adding 5 µl of cell suspension to the sgRNA/RNP solution, which was then electroporated using a Lonza 4D-Nucleofector. Cells were immediately resuspended in 2 ml of fresh media and transferred to 12-well plates. Cells were incubated for 72 h and collected for DNA isolation and Sanger sequencing for verification of gene editing. Sanger sequencing results were analyzed using Synthego's Inference of CRISPR Edits (ICE) tools, and clonal expansion was initiated after confirmation of gene editing. The following control and guide RNAs to knockout *FAM43A* were used: 5′-CACCGGTATTACTGATATTGGTGGG-3′ (control), 5′-CGGCGCUCAGCUCGCUGGCG-3′, 5′-GAAGCUGCACAUCACUAGCG-3′, and 5′-ACCAUCCAGGCGCGCGGCGA-3′.

EdU incorporation assay and growth curve generation

EdU experiments were performed using the Alexa Fluor 488 Click-It EdU kit (#C10637; Thermo Fisher Scientific) according to the manufacturer's protocol. Briefly, 5,000 cells were plated on coverslips in a 12-well plate in 1 ml of EMEM + 10% (vol/vol) FBS. For samples treated with 96 h of ddC, ddC was added 8 h following cell seeding. For cells treated for 48 h, ddC was added 2 days following seeding. 72 h following cell seeding, half of the cell culture media (500 µl) was removed and replaced with fresh 500 µl of EMEM +10% (vol/vol) FBS containing 20 µM EdU (final concentration of 10 µM) and ddC (final concentration of 20 µM). Cells were incubated for 24 h in the presence of EdU and fixed with 4% paraformaldehyde in PBS. After fixation, cells were permeabilized with 0.2% (vol/vol) Triton X-100 in PBS at room temperature for 10 min. Cells were washed twice with 1 ml of 3% (wt/vol) bovine serum albumin (BSA) (A9647; Sigma-Aldrich) in PBS before proceeding with a 30-min click reaction following the manufacturer's protocol. The reaction mixture was removed and nuclei were stained with Hoechst (1:1,000 in PBS; 2037341; Invitrogen) for 30 min at room temperature. Cells were washed twice with PBS and coverslips were mounted on slides using Prolong Glass (P3680; Invitrogen). The following day, fixed cells were imaged on the EVOS M5000 imaging system (Thermo Fisher Scientific) equipped with a 3.2 MP monochrome CMOS camera using a 20× 0.40NA objective. The percent of EdU-positive nuclei was quantified using the Cell Count function in Fiji (version 2.14.0/1.54f; Image J, NIH) (Schindelin et al., 2012) (EdU-positive nuclei/total nuclei per image). For growth curve generation, the population doubling after each passage was quantified using the following equation: $\mathrm{Log}_2(D/D0)$, where D = density at passaging and D0 = seeding density.

Pulse EdU labeling and quantification of replicating mtDNA

Pulse EdU labeling to measure mtDNA replication was performed as described above with the following modifications: cells were incubated with 10 µM EdU for 4 h, and two sequential 1-h click reactions were performed following fixation and permeabilization. The click reaction was removed, coverslips were washed 2 × 5 min with PBS and immunofluorescence was conducted as described in the "Immunofluorescence" section using the following primary antibodies: mouse anti-DNA (1:200, CBL186; Millipore, RRID: AB_11213573) and chicken anti-HSP60 (1:1,000, CPCA-HSP60; EnCor Biotechnology, RRID: AB_2572330). For quantification of replicating mtDNA nucleoids, segmentation of single-channel maximum intensity z projections was performed using the Ilastik software (version 1.4.0) segmentation workflow (pixel classification) (Horvath et al., 2011). Segmented single-channel images were further analyzed using the Fiji Analyze Particles plugin to acquire the number of anti-DNA and EdU double-positive particles that colocalize with mitochondria. The percentage of EdU-positive nucleoids was then determined as a measurement of mtDNA replication.

H_2O_2 and ATP measurements

For H_2O_2 measurements, cells were plated at a density of 1.8×10^5 in 6-well plates. Cells were treated with ddC for 72 or 24 h before being trypsinized, counted, and plated on white-walled 96 well plates at a density of five thousand cells/well in a ddC-containing medium (20 µM). 24 h later, a subset of untreated cells was treated with H_2O_2 (180 µM) (H1009; Sigma-Aldrich) for 1 h as a positive control. Whole-cell H_2O_2 was measured using the ROS-Glo H_2O_2 Assay Kit (G8820; Promega) according to the manufacturer's instructions. For ATP measurements, cells were plated and maintained as previously described, and whole-cell ATP was measured using the ATP Detection Assay Kit (700410; Cayman Chemical) according to the manufacturer's instructions. Luminescence was measured using the TECAN Infinite 200 Pro plate reader (TECAN). Following measurements, cells were lysed in 1X RIPA buffer (9806; Cell Signaling Technology) supplemented with a 1X protease/phosphatase inhibitor cocktail (5872S; Cell Signaling Technology). Protein concentration was quantified using the Pierce BCA Protein Assay Kit (23209; Cell Signaling Technology) for normalization.

Mitochondrial mass and membrane potential measurements

IMR90 cells were plated in triplicates in 6-well plates at 200–300k cells/well. Cells were incubated in serum-free media (EMEM without FBS) for 20 min at 37°C. Cells were then stained with 100 nM MitoTracker Green FM (M7514; Thermo Fisher Scientific) to assess mitochondrial mass and 100 nM TMRE (tetramethylrhodamine, ethyl ester) (T669; Thermo Fisher Scientific) to determine mitochondrial membrane potential in serum-free media for 30 min at 37°C. Cells were washed in PBS, trypsinized, transferred to Eppendorf tubes, spun down, and resuspended in 150 µl of FACS buffer (PBS + 2% [vol/vol] FBS) plus LIVE/DEAD Fixable Aqua (1: 1,000, L34957; Thermo Fisher Scientific). Data were collected on a BD FACSymphony A3 Cell Analyzer (BD Biosciences) and analyzed with FlowJo Software (BD Biosciences, version 10.8.0). Dead cells and doublets were gated out, and the mean fluorescent intensity (MFI) for each dye was determined and normalized to the control. At least 10k cells were collected and analyzed for each sample. The following channels were used for measurements: TMRE: PE (red) channel, MTG: FITC/GFP/ BB515 (green) channel, and Live/Dead Aqua: BV510 (BV480 on the A3) channel.

Ratiometric flow cytometry to measure mitophagy flux

Plasmid pHAGE-mt-mKeima (2 µg) was cotransfected into Lenti-X-293T cells as described in the "Lentivirus generation, cell transduction, and siRNA transfection" section to generate lentiviral particles. IMR90 cells were transduced and, 48 h after transduction, transfected with the indicated siRNA. After 72 h, control (siCtrl) cells were treated with 20 µM CCCP (25458; Cayman Chemical), 1 mM Deferiprone (20387; Cayman Chemical), or 50 µM CQ (14194; Cayman Chemical) to induce or block basal mitophagy. 96 h after transfection, cells were washed with PBS, trypsinized, and transferred to Eppendorf tubes, spun down, and resuspended in 150 µl of FACS buffer plus Zombie Violet Fixable Viability kit (423113; BioLegend). Data were analyzed with FlowJo Software (version 10.8.0; BD Biosciences). Briefly, dead cells and doublets were gated out. A non-transduced control was used to gate out mKeima-negative cells, and CCCP and DFP samples were used as positive controls. At least 10,000 cells were collected and analyzed for each sample. The following channels were used for measurement: BV605, PE-CF594, and BV421.

Seahorse analysis

Cells treated with ddC (20 µM) for 72 or 24 h were seeded at a density of 10,000 cells/well in Agilent Seahorse XFe96 microplates (101085-004) (4 wells/condition). The following day, oxygen consumption measurements were measured using a Seahorse XF96 analyzer (Agilent). Cells were equilibrated in serum-free Seahorse XF base medium without phenol red (Agilent) supplemented with 5 mM glucose (MilliporeSigma), 2 mM glutamine (Thermo Fisher Scientific), and 1 mM pyruvate (Thermo Fisher Scientific) for 1 h in a non-CO_2 incubator at 37°C before starting the assay. The order and final concentration of the injected compounds were as follows: Oligomycin (75351; Sigma-Aldrich) (1.5 µM), CCCP (25458; Cayman Chemicals) (2 µM), Rotenone (R8875; Sigma-Aldrich), and Antimycin (A8674; Sigma-Aldrich) (0.5 µM each). Following oxygen consumption measurements, cells were lysed in 1X RIPA buffer supplemented with a 1X protease/phosphatase inhibitor cocktail, and protein was measured using the Pierce BCA Protein Assay Kit for normalization. Data were analyzed using the Wave software version 2.6.1 (Agilent) and normalized to protein content.

mtDNA copy number assessment

Cell pellets were resuspended in 50 mM NaOH and incubated for 30 min at 95°C, followed by neutralization by 1/10 volume of 1 M Tris-HCl (pH 8.0). DNA samples were diluted to 10 ng/µl in DNase-free water and subjected to qPCR analysis using the following primers (Eton Biosciences) to amplify mtDNA and nuclear DNA; human *B2M*-F 5′-CTTTCTGGCTGGATTGGTATCT-3′, human *B2M*-R 5′-CAGAATAGGCTGCTGTTCCTAC-3′, human *ND1*-F 5′-TCTCACCATCGCTCTTCTACT-3′, human *ND1*-R 5′-AGGCTAGAGGTGGCTAGAATAA-3′, mouse *Tert*-F 5′-CTAGCTCATGTGTCAAGACCCTCTT-3′, mouse *Tert*-R 5′-GCCAGCACGTTTCTCTCGTT-3′, mouse *ND1*-F 5′-CTAGCAGAAACAAACCGGGC-3′, and mouse *ND1*-R 5′-CCGGCTGCGTATTCTACGTT-3′. Three technical replicates were analyzed for each biological sample and normalized against the nuclear control value (*B2M* for human samples and *Tert* for mouse samples). Relative mtDNA copy number (%) was analyzed using a 2−ΔΔCt method, and the control mtDNA copy number was given a value of 100%.

Immunoblotting

Cells from one confluent 6-cm dish were trypsinized and pelleted in 1.5 ml Eppendorf tubes. The cell pellet was lysed in 1X RIPA buffer supplemented with a 1X protease/phosphatase inhibitor cocktail. Samples were incubated on ice for 30 min with intermittent vortexing and spun down at 13,000 × *g* for 10 min at 4°C. Protein concentration was quantified using the Pierce BCA Protein Assay Kit. Protein (20–30 µg) were separated by SDS-polyacrylamide gel electrophoresis and subsequently transferred to a PVDF membrane (IPVH00010; MilliporeSigma) at 100V for 60 min at 4°C. After transfer, membranes were stained with Ponceau S (14330; Cayman Chemical Company) to ensure accurate loading before being washed and blocked in 4% (wt/vol) BSA in tris-buffered saline with Tween 20 (TBS-T) for 1 h at room temperature. Membranes were incubated with primary antibodies overnight at 4°C on a shaker. The following antibodies were used for immunoblotting at a 1:1,000 dilution unless otherwise indicated: rabbit anti-beta ACTIN (Cat# 5125; Cell Signaling Technology, RRID: AB_1903890), rabbit anti-ATG12 (Cat# 4180; Cell Signaling Technology, RRID: AB_1903898), rabbit anti-ATG7 (Cat# 8558; Cell Signaling Technology, RRID: AB_10831194), rabbit anti-ATG5 (Cat# 12994; Cell Signaling Technology, RRID: AB_2630393), rabbit anti-CHK2 (Cat# 2662; Cell Signaling Technology, RRID: AB_2080793, 1:500 dilution), rabbit anti-p^{T68}CHK2 (Cat# 2197; Cell Signaling Technology, RRID: AB_2080501, 1:500 dilution), rabbit anti-LC3a/b (Cat# 12741; Cell Signaling Technology, RRID: AB_2617131), rabbit anti-RRM1 (Cat# 8637; Cell Signaling Technology, RRID: AB_11217623), rabbit anti-p53R2 (Cat# ab8105; Abcam, RRID: AB_306275), rabbit anti-TFAM (Cat# 22586-1-AP; Proteintech, RRID: AB_11182588), rabbit anti-PGC-1α (Cat# NBP1-04676R; Novus Biologicals, RRID: AB_1850632), mouse anti-OXPHOS cocktail (Cat# ab110411; Abcam, RRID: AB_2756818, 1:500 dilution), and goat anti-p16INK4a (p16) (Cat# AF5779; R and D Systems, RRID: AB_1964666, 1:500 dilution). Following overnight incubation with the indicated primary antibodies, membranes were subjected to three 5-min washes with TBS-T and incubated with the appropriate secondary antibody in 4% BSA for 45 min at room temperature. The following HRP-linked secondary antibodies were used at a 1:10,000 dilution: HRP-conjugated anti-rabbit (Cat #7074; Cell Signaling Technology, RRID: AB_2099233), anti-mouse (Cat #7076; Cell Signaling Technology, RRID: AB_330924), and anti-goat (Cat #ab6885; Abcam, RRID: AB_955423). Membranes were developed with ProSignal Femto Reagent (20-302; Genesee Scientific) with the ChemiDoc MP Imaging System (Bio-Rad Laboratories). Western blots were quantified using Fiji, with normalization to both β-actin and the control condition, and control samples were given a value of 1.

Reverse transcription-quantitative PCR (RT-qPCR)

Total RNA was extracted using the RNeasy Plus Mini Kit according to the manufacturer's instructions with the following modifications: all optional steps were performed during RNA extraction, and elution time was extended to 5 min to improve yield. Reverse transcription was done using the High-Capacity cDNA Kit (4368814; Thermo Fisher Scientific) with 1–2 µg of RNA input per reaction. Equal amounts of cDNA and the indicated primers were used for RT-qPCR using the Fast SYBR Green Master Mix (4364346; Thermo Fisher Scientific) on the CFX384 Touch Real-Time PCR Detection System (Bio-Rad Laboratories). Technical triplicates were assessed for each biological replicate and normalized against the beta-actin threshold cycle (Ct) value to calculate ΔCt. The ΔCt of each sample was compared to the ΔCt of the control sample to generate the ΔΔCt value. The relative mRNA expression for each target was then analyzed using the $2^{\Delta\Delta Ct}$ method, and the fold change was plotted relative to control samples, which were given a value of 1. The following human primers (Eton Bioscience) were used: *ACTIN*-F 5′-ACTGGAACGGTGAAAGGTGAC-3′, *ACTIN*-R 5′-AGAGAAGTGGGGTGGCTTTT-3′, *FAM43A*-F 5′-GTGCGGGGACTTGTTGGATAC-3′, *FAM43A*-R 5′-CCCAGGTCGCTAATAAGTTGC-3′, *CHEK2*-F 5′-TGAGAACCTTATGTGGAACCCC-3′, *CHEK2*-R 5′-ACAGCACGGTTATACCCAGC-3′, *RRM1*-F 5′-GCCAGGATCGCTGTCTCTAAC-3′, *RRM1*-R 5′-GAGAGTGTTTGCCATTATGTGGA-3′, *RRM2*-F 5′-CGCTGGATTGGGGACAAAGA-3′, *RRM2*-R 5′-CCAGGCATCAGTCCTCGTTT-3′, *RRM2B*-F 5′-CCTTGCGATGGATAGCAGATAG-3′, *RRM2B*-R 5′-GCCAGAATATAGCAGCAAAAGATC-3′. The following mouse primers (Eton Bioscience) were used: *Actin*-F 5′-ATGCTCCCCGGGCTGTAT-3′, *Actin*-R 5′-CATAGGAGTCCTTCTGACCCATTC-3′, *Fam43a*-F 5′-TGGGCAAGATCTGGAGCAAG-3′, *Fam43a*-R 5′-CGGTATACCCAGGCGAAGAC-3′.

RNA sequencing and analysis

Total RNA was extracted using the RNeasy Plus Mini Kit (74136; Qiagen) according to the manufacturer's instructions with the following modifications: all optional steps were performed during RNA extraction, and elution time was extended to 5 min to improve yield. The RNA quality was analyzed by RNA screen tape (Agilent). RNA sequencing was performed using the Illumina HiSeq 2500 platform on 50-bp single-end libraries prepared using the Illumina TruSeq RNA sample preparation kit (20020594; Illumina). Reads were mapped and aligned to the human genome GRCh38.p13 using STAR v2.5.3a and then quantified using HOMER to generate normalized raw counts (Table S1). DESeq2 was used to identify differentially expressed genes at each timepoint relative to untreated controls (defined by $\log_2$ fold change of >0.58 and less than -0.58 and P value <0.05). A heatmap of the significantly differentially expressed genes at 96 h was generated to show the expression of these genes at different time points relative to untreated controls (Table S2). Overrepresentation analysis was performed using WebGestalt's "transcription factor network" functional databases (Table S3). The analysis was performed on differentially expressed genes at 96 h of ddC treatment (Table S3). Raw sequencing data is available at the Gene Expression Omnibus (GEO) under accession code GSE273181.

Immunofluorescence

Cells grown on coverslips were fixed at 37°C using a prewarmed (37°C) solution of 4% paraformaldehyde in PBS for 15 min and permeabilized with 0.1% (vol/vol) Triton X-100 in PBS at room temperature for 15 min. Coverslips were then blocked in filtered PBS containing 1% (wt/vol) BSA at room temperature for 1 h and incubated with primary antibodies diluted in blocking buffer overnight at 4°C. The following primary antibodies were used at the indicated dilutions: FAM43A-FITC (1:200, TR36978; Tresars), chicken anti-HSP60 (1:1,000, Cat #CPCA-HSP60; EnCor Biotechnology, RRID: AB_2572330), rabbit anti-LC3a/b (1:100, Cat #12741; Cell Signaling Technology, RRID: AB_2617131), rabbit anti-LAMP1 (1:500, Cat #9091S; Cell Signaling Technology, RRID: AB_2687579, 1:500), rabbit anti-GIANTIN (1:1,000, Cat #ab80864; Abcam, RRID: AB_10670397), mouse anti-dsDNA (1:200CBL186; Millipore, RRID: AB_11213573), mouse anti-Histone H2A.X pSer139 (γH2AX) (1:250Cat #05-636; Millipore, RRID: AB_309864), and rabbit anti-53BP1 (1:500, Cat #NB100-304; Novus Biologicals, RRID: AB_10003037). Coverslips were subsequently washed with PBS and incubated with the corresponding secondary antibodies (1:500 in blocking buffer) for 1 h at room temperature. The following secondary antibodies were used: goat anti-chicken Alexa Fluor 647 (Cat #ab150171; Abcam, RRID: AB_2921318), donkey anti-rabbit Alexa Fluor 568

(Cat #A-10042; Thermo Fisher Scientific, RRID: AB_2534017), donkey anti-mouse Alexa Fluor 488 (Cat #A-21202; Thermo Fisher Scientific, RRID: AB_141607), and donkey anti-mouse Alexa Fluor 568 (Cat #A-10037; Thermo Fisher Scientific, RRID: AB_11180865). The secondary antibody was removed by 4 × 5-min washes in PBS. If nuclei were stained, coverslips were incubated with Hoechst diluted (1:2,000) in PBS for 20 min, followed by two 5-min washes with PBS. Coverslips were then mounted onto slides using Prolong Glass Antifade Mountant (P36980; Invitrogen) and allowed to dry for 24 h prior to imaging.

Spinning disk and Airyscan imaging

For spinning disk imaging, fixed cells were imaged with a Zeiss CSU spinning disk confocal microscope with a Confocal Scanner Unit-X1 Yokogawa spinning disk scan head on a Prime 95B scientific complementary metal oxide semiconductor (sCMOS) camera (Teledyne Photometrics) using an inverted Plan-Apochromat 63×/1.4 NA oil objective. For Airyscan imaging, fixed cells were imaged with a Plan-Apochromat 63×/1.4 NA oil objective on an upright Zeiss 880 Rear Port Laser Scanning Confocal and Airyscan FAST Microscope. Airyscan data were processed using Zen Black (version 2.3; Zeiss). All spinning disk and Airyscan images are shown as maximum intensity z projections. Spinning disk and Airyscan images are denoted as such in all figure legends. The total cell intensity of the FAM43A-FITC signal was quantified using Fiji software. Briefly, cells of interest were outlined using the drawing/selection tool. Under the Analyze tab's "set measurements" menu, the area integrated intensity and mean grey value were selected, and the area's mean fluorescence was measured. Using the drawing tool, the background mean fluorescence was measured by drawing a circle in an empty image region. The corrected total cell fluorescence (CTCF) was calculated using the following formula: CTCF = integrated density − (area of selected cell × mean fluorescence of background reading). For FAM43A aggregate quantification, segmentation of maximum intensity z projections was performed using the Ilastik software segmentation workflow (pixel classification) to distinguish individual FAM43A positive structures from background regions (Horvath et al., 2011). The segmented images were then processed using the Ilastik Object classification workflow (Inputs: Raw data, segmentation) and used to classify and count FAM43A puncta and aggregates. Colocalization of FAM43A and organelle markers was performed using the JaCop v2.0 plugin in Fiji (M1 & M2 coefficients, Costes' automatic threshold). The Manders coefficient (M1-percentage of pixels on FAM43A channel that overlap with pixels in channel displaying organelle markers) was used for analysis.

Statistical analysis

GraphPad Prism 9 software (version 9.5.1) was used for all statistical analysis and graph generation. All experiments were conducted at least twice. Data obtained from biological replicates were combined where indicated for statistical analysis. Results were analyzed using unpaired, two-tailed Student's *t* test or one-way ANOVA with Dunnett's multiple comparisons. Data are represented as mean values and error bars represent SD unless otherwise indicated in the figure legends. The P values are indicated by *$P < 0.05$, **$P < 0.01$, ***$P < 0.001$, and ****$P < 0.0001$. $P > 0.05$ was considered to be not significant (ns).

Online supplemental material

Fig. S1 shows the kinetics of mtDNA depletion and repletion and the effect of mtDNA depletion on cell proliferation and OXPHOS complex abundance. Fig. S2 shows the localization of FAM43A in untreated and ddC-treated cells. Fig. S3 shows the activation of autophagy and mitophagy in *FAM43A*-knockdown cells. Fig. S4 shows measurements of nuclear DNA damage in *FAM43A*-knockdown cells and supporting RT-qPCR data for Fig. 5. Table S1 shows normalized gene counts from RNA-seq analysis of IMR90 cells treated with vehicle (water) or ddC for 24, 48, 72, or 96 h. Table S2 shows a list of differentially expressed genes from RNA-seq of IMR90 cells treated with ddC for 96 h and the expression of these genes at all other time points assayed (values used for Fig. 2 A). Table S3 shows the enriched transcription factor networks in IMR90 cells treated with ddC for 96 h.

Data availability

Sequencing data (bulk RNA-seq) generated in this study is available at the GEO repository under the accession code GSE273181. All the data are available in the main text or the supplementary materials. Other materials generated in this manuscript are available from the corresponding author upon reasonable request and, when applicable, fulfillment of the appropriate material transfer agreements.

Acknowledgments

The authors thank Dr. Christina Towers for the kind gift of WT and *ATG7* knockout H292 cells and all members of the Shadel Lab for their support and advice.

This work in the Shadel and Shaw labs was supported by the following National Institutes of Health (NIH) grants: R01 CA228211 and P01 AG073084 to G.S. Shadel, R01 CA234047 and R35 CA220538 to R.J. Shaw, F31 AG062099 to A.G. Sainz, T32 CA009370-39 (supporting A.G. Moyzis), and T32 GM007198 (supporting M.P. Donnelly). G.S. Shadel also holds the Audrey Geisel Chair in Biomedical Science and also supported by the Spruance Foundation II. A.G. Moyzis was supported by CRI Irvington postdoctoral fellowship CRI4122, K.C. Mangalhara by the Salkexcellerators postdoctoral fellowship, P.B. Esparza-Moltó by fellowships from Fundación Alfonso Martín Escudero (Madrid, Spain) and the Paul F. Glenn Center for Biology of Aging Research at the Salk Institute. Support for the Salk NGS, TGC, BPHO and FCCF core facilities used for this study was provided by NIH-NCI Cancer Center Support Grant P30 014195, NIH-NIA P30 AG068635 (San Diego Nathan Shock Center of Excellence in the Basic Biology of Aging), Shared Instrumentation Grant S10-OD023689, the Helmsley Trust, and the Waitt Foundation.

Author contributions: A.G. Sainz: Conceptualization, Data curation, Formal analysis, Investigation, Methodology, Validation, Visualization, Writing - original draft, Writing - review &

editing, G.R. Rojas: Investigation, Resources, Writing - review & editing, A.G. Moyzis: Investigation, Writing - review & editing, M.P. Donnelly: Investigation, K.C. Mangalhara: Investigation, M.A. Johnson: Formal analysis, Investigation, P.B. Esparza-Moltó: Investigation, Methodology, Writing - review & editing, K.J. Grae: Investigation, R.J. Shaw: Conceptualization, Writing - review & editing, G.S. Shadel: Conceptualization, Funding acquisition, Project administration, Resources, Supervision, Writing - original draft, Writing - review & editing.

Disclosures: The authors declare no competing interests exist.

Submitted: 17 November 2023
Revised: 4 October 2024
Accepted: 10 December 2024

References

Aman, Y., T. Schmauck-Medina, M. Hansen, R.I. Morimoto, A.K. Simon, I. Bjedov, K. Palikaras, A. Simonsen, T. Johansen, N. Tavernarakis, et al. 2021. Autophagy in healthy aging and disease. *Nat. Aging*. 1:634–650. https://doi.org/10.1038/s43587-021-00098-4

Aye, Y., M. Li, M.J.C. Long, and R.S. Weiss. 2015. Ribonucleotide reductase and cancer: Biological mechanisms and targeted therapies. *Oncogene*. 34: 2011–2021. https://doi.org/10.1038/onc.2014.155

Bensalem, J., K.J. Hattersley, L.K. Hein, X.T. Teong, J.M. Carosi, S. Hassiotis, R.H. Grose, C. Fourrier, L.K. Heilbronn, and T.J. Sargeant. 2021. Measurement of autophagic flux in humans: An optimized method for blood samples. *Autophagy*. 17:3238–3255. https://doi.org/10.1080/15548627.2020.1846302

Bomba-Warczak, E., S.L. Edassery, T.J. Hark, and J.N. Savas. 2021. Long-lived mitochondrial cristae proteins in mouse heart and brain. *J. Cell Biol.* 220: e202005193. https://doi.org/10.1083/jcb.202005193

Butow, R.A., and N.G. Avadhani. 2004. Mitochondrial signaling: The retrograde response. *Mol. Cell*. 14:1–15. https://doi.org/10.1016/S1097-2765(04)00179-0

Chandiramani, N., X. Wang, and M. Margeta. 2011. Molecular basis for vulnerability to mitochondrial and oxidative stress in a neuroendocrine CRI-G1 cell line. *PLoS One*. 6:e14485. https://doi.org/10.1371/journal.pone.0014485

Chen, C.H., and Y.C. Cheng. 1989. Delayed cytotoxicity and selective loss of mitochondrial DNA in cells treated with the anti-human immunodeficiency virus compound 2′,3′-dideoxycytidine. *J. Biol. Chem.* 264:11934–11937. https://doi.org/10.1016/S0021-9258(18)80156-9

Chen, L., D.M. Gilkes, Y. Pan, W.S. Lane, and J. Chen. 2005. ATM and Chk2-dependent phosphorylation of MDMX contribute to p53 activation after DNA damage. *EMBO J.* 24:3411–3422. https://doi.org/10.1038/sj.emboj.7600812

Chen, L.H., W.-H. Kuo, M.-H. Tsai, P.-C. Chen, C.K. Hsiao, E.Y. Chuang, L.-Y. Chang, F.-J. Hsieh, L.-C. Lai, and K.-J. Chang. 2011. Identification of prognostic genes for recurrent risk prediction in triple negative breast cancer patients in Taiwan. *PLoS One*. 6:e28222. https://doi.org/10.1371/journal.pone.0028222

Chen, W., H. Zhao, and Y. Li. 2023. Mitochondrial dynamics in health and disease: Mechanisms and potential targets. *Signal Transduct. Target. Ther.* 8:333. https://doi.org/10.1038/s41392-023-01547-9

Crider, D.G., L.J. García-Rodríguez, P. Srivastava, L. Peraza-Reyes, K. Upadhyaya, I.R. Boldogh, and L.A. Pon. 2012. Rad53 is essential for a mitochondrial DNA inheritance checkpoint regulating G1 to S progression. *J. Cell Biol.* 198:793–798. https://doi.org/10.1083/jcb.201205193

Dagsgaard, C., L.E. Taylor, K.M. O'Brien, and R.O. Poyton. 2001. Effects of anoxia and the mitochondrion on expression of aerobic nuclear COX genes in yeast: Evidence for a signaling pathway from the mitochondrial genome to the nucleus. *J. Biol. Chem.* 276:7593–7601. https://doi.org/10.1074/jbc.M009180200

Eaton, J.S., Z.P. Lin, A.C. Sartorelli, N.D. Bonawitz, and G.S. Shadel. 2007. Ataxia-telangiectasia mutated kinase regulates ribonucleotide reductase and mitochondrial homeostasis. *J. Clin. Invest.* 117:2723–2734. https://doi.org/10.1172/JCI31604

Eisenberg-Bord, M., and M. Schuldiner. 2017. Ground control to major TOM: Mitochondria-nucleus communication. *FEBS J.* 284:196–210. https://doi.org/10.1111/febs.13778

Formichi, P., N. Cardone, I. Taglia, E. Cardaioli, S. Salvatore, A.L. Gerfo, C. Simoncini, V. Montano, G. Siciliano, M. Mancuso, et al. 2020. Fibroblast growth factor 21 and grow differentiation factor 15 are sensitive biomarkers of mitochondrial diseases due to mitochondrial transfer-RNA mutations and mitochondrial DNA deletions. *Neurol. Sci.* 41:3653–3662. https://doi.org/10.1007/s10072-020-04422-5

Freeman, A.K, V. Dapic, and A.N.A Monteiro. 2010. Negative regulation of CHK2 activity by protein phosphatase 2A is modulated by DNA damage. *Cell Cycle*. 9:736–747. https://doi.org/10.4161/cc.9.4.10613

Fu, Y., O. Sacco, E. DeBitetto, E. Kanshin, B. Ueberheide, and A. Sfeir. 2023. Mitochondrial DNA breaks activate an integrated stress response to reestablish homeostasis. *Mol. Cell*. 83:3740–3753.e9. https://doi.org/10.1016/j.molcel.2023.09.026

Fumagalli, M., D. Ronchi, M.F. Bedeschi, A. Manini, G. Cristofori, F. Mosca, R. Dilena, M. Sciacco, S. Zanotti, D. Piga, et al. 2022. A novel RRM2B mutation associated with mitochondrial DNA depletion syndrome. *Mol. Genet. Metab. Rep.* 32:100887. https://doi.org/10.1016/j.ymgmr.2022.100887

Greaves, L.C., A.K. Reeve, R.W. Taylor, and D.M. Turnbull. 2012. Mitochondrial DNA and disease. *J. Pathol.* 226:274–286. https://doi.org/10.1002/path.3028

Guittet, O., P. Håkansson, N. Voevodskaya, S. Fridd, A. Gräslund, H. Arakawa, Y. Nakamura, and L. Thelander. 2001. Mammalian p53R2 protein forms an active ribonucleotide reductase in vitro with the R1 protein, which is expressed both in resting cells in response to DNA damage and in proliferating cells. *J. Biol. Chem.* 276:40647–40651. https://doi.org/10.1074/jbc.M106088200

Guo, J.Y., X. Teng, S.V. Laddha, S. Ma, S.C. Van Nostrand, Y. Yang, S. Khor, C.S. Chan, J.D. Rabinowitz, and E. White. 2016. Autophagy provides metabolic substrates to maintain energy charge and nucleotide pools in Ras-driven lung cancer cells. *Genes Dev.* 30:1704–1717. https://doi.org/10.1101/gad.283416.116

Gustafsson, C.M., M. Falkenberg, and N.-G. Larsson. 2016. Maintenance and expression of mammalian mitochondrial DNA. *Annu. Rev. Biochem.* 85: 133–160. https://doi.org/10.1146/annurev-biochem-060815-014402

Horvath, P., T. Wild, U. Kutay, and G. Csucs. 2011. Machine learning improves the precision and robustness of high-content screens: Using nonlinear multiparametric methods to analyze screening results. *SLAS Discov.* 16: 1059–1067. https://doi.org/10.1177/1087057111414878

Huttlin, E.L., R.J. Bruckner, J. Navarrete-Perea, J.R. Cannon, K. Baltier, F. Gebreab, M.P. Gygi, A. Thornock, G. Zarraga, S. Tam, et al. 2021. Dual proteome-scale networks reveal cell-specific remodeling of the human interactome. *Cell*. 184:3022–3040.e28. https://doi.org/10.1016/j.cell.2021.04.011

Klionsky, D.J., K. Abdelmohsen, A. Abe, M.J. Abedin, H. Abeliovich, A. Acevedo Arozena, H. Adachi, C.M. Adams, P.D. Adams, K. Adeli, et al. 2016. Guidelines for the use and interpretation of assays for monitoring autophagy. *Autophagy*. 8:445–544. https://doi.org/10.4161/auto.19496

Koczor, C.A., I.N. Shokolenko, A.K. Boyd, S.P. Balk, G.L. Wilson, and S.P. LeDoux. 2009. Mitochondrial DNA damage initiates a cell cycle arrest by a Chk2-associated mechanism in mammalian cells. *J. Biol. Chem.* 284: 36191–36201. https://doi.org/10.1074/jbc.M109.036020

Krishna, S., R. Arrojo E Drigo, J.S. Capitanio, R. Ramachandra, M. Ellisman, and M.W. Hetzer. 2021. Identification of long-lived proteins in the mitochondria reveals increased stability of the electron transport chain. *Dev. Cell*. 56:2952–2965.e9. https://doi.org/10.1016/j.devcel.2021.10.008

Kumar, M., S. Michael, J. Alvarado-Valverde, B. Mészáros, H. Sámano-Sánchez, A. Zeke, L. Dobson, T. Lazar, M. Örd, A. Nagpal, et al. 2022. The eukaryotic linear motif resource: 2022 release. *Nucleic Acids Res.* 50: D497–D508. https://doi.org/10.1093/nar/gkab975

Larsson, N.G., J. Wang, H. Wilhelmsson, A. Oldfors, P. Rustin, M. Lewandoski, G.S. Barsh, and D.A. Clayton. 1998. Mitochondrial transcription factor A is necessary for mtDNA maintenance and embryogenesis in mice. *Nat. Genet.* 18:231–236. https://doi.org/10.1038/ng0398-231

Lebedeva, M.A., and G.S. Shadel. 2007. Cell cycle- and ribonucleotide reductase-driven changes in mtDNA copy number influence mtDNA Inheritance without compromising mitochondrial gene expression. *Cell Cycle*. 6:2048–2057. https://doi.org/10.4161/cc.6.16.4572

Liu, L., Y. Li, J. Wang, D. Zhang, H. Wu, W. Li, H. Wei, N. Ta, Y. Fan, Y. Liu, et al. 2021. Mitophagy receptor FUNDC1 is regulated by PGC-1α/NRF1 to fine tune mitochondrial homeostasis. *EMBO Rep.* 22:e50629. https://doi.org/10.15252/embr.202050629

Martínez-Reyes, I., and N.S. Chandel. 2020. Mitochondrial TCA cycle metabolites control physiology and disease. *Nat. Commun.* 11:102. https://doi.org/10.1038/s41467-019-13668-3

Matsuoka, S., G. Rotman, A. Ogawa, Y. Shiloh, K. Tamai, and S.J. Elledge. 2000. Ataxia telangiectasia-mutated phosphorylates Chk2 in vivo and in vitro. *Proc. Natl. Acad. Sci. USA*. 97:10389–10394. https://doi.org/10.1073/pnas.190030497

Mauthe, M., I. Orhon, C. Rocchi, X. Zhou, M. Luhr, K.-J. Hijlkema, R.P. Coppes, N. Engedal, M. Mari, and F. Reggiori. 2018. Chloroquine inhibits autophagic flux by decreasing autophagosome-lysosome fusion. *Autophagy*. 14:1435–1455. https://doi.org/10.1080/15548627.2018.1474314

McShane, M.A., S.R. Hammans, M. Sweeney, I.J. Holt, T.J. Beattie, E.M. Brett, and A.E. Harding. 1991. Pearson syndrome and mitochondrial encephalomyopathy in a patient with a deletion of mtDNA. *Am. J. Hum. Genet.* 48:39–42.

Medeiros, T.C., R.L. Thomas, R. Ghillebert, and M. Graef. 2018. Autophagy balances mtDNA synthesis and degradation by DNA polymerase POLG during starvation. *J. Cell Biol.* 217:1601–1611. https://doi.org/10.1083/jcb.201801168

Neill, T., A. Torres, S. Buraschi, R.T. Owens, J.B. Hoek, R. Baffa, and R.V. Iozzo. 2014. Decorin induces mitophagy in breast carcinoma cells via peroxisome proliferator-activated receptor γ coactivator-1α (PGC-1α) and mitostatin. *J. Biol. Chem.* 289:4952–4968. https://doi.org/10.1074/jbc.M113.512566

Newman, L.E., and G.S. Shadel. 2023. Mitochondrial DNA release in innate immune signaling. *Annu. Rev. Biochem.* 92:299–332. https://doi.org/10.1146/annurev-biochem-032620-104401

Niu, R., M. Yoshida, and F. Ling. 2012. Increases in mitochondrial DNA content and 4977-bp deletion upon ATM/Chk2 checkpoint activation in HeLa cells. *PLoS One*. 7:e40572. https://doi.org/10.1371/journal.pone.0040572

Parikh, V.S., M.M. Morgan, R. Scott, L.S. Clements, and R.A. Butow. 1987. The mitochondrial genotype can influence nuclear gene expression in yeast. *Science*. 235:576–580. https://doi.org/10.1126/science.3027892

Park, S.Y., B. Choi, H. Cheon, Y.K. Pak, M. Kulawiec, K.K. Singh, and M.S. Lee. 2004. Cellular aging of mitochondrial DNA-depleted cells. *Biochem. Biophys. Res. Commun.* 325:1399–1405. https://doi.org/10.1016/j.bbrc.2004.10.182

Ploumi, C., I. Daskalaki, and N. Tavernarakis. 2017. Mitochondrial biogenesis and clearance: A balancing act. *FEBS J.* 284:183–195. https://doi.org/10.1111/febs.13820

Pontarin, G., P. Ferraro, L. Bee, P. Reichard, and V. Bianchi. 2012. Mammalian ribonucleotide reductase subunit p53R2 is required for mitochondrial DNA replication and DNA repair in quiescent cells. *Proc. Natl. Acad. Sci. USA*. 109:13302–13307. https://doi.org/10.1073/pnas.1211289109

Rossignol, R., B. Faustin, C. Rocher, M. Malgat, J.-P. Mazat, and T. Letellier. 2003. Mitochondrial threshold effects. *Biochem. J.* 370:751–762. https://doi.org/10.1042/bj20021594

Ryan, M.T., and N.J. Hoogenraad. 2007. Mitochondrial-nuclear communications. *Annu. Rev. Biochem.* 76:701–722. https://doi.org/10.1146/annurev.biochem.76.052305.091720

Schindelin, J., I. Arganda-Carreras, E. Frise, V. Kaynig, M. Longair, T. Pietzsch, S. Preibisch, C. Rueden, S. Saalfeld, B. Schmid, et al. 2012. Fiji: An open-source platform for biological-image analysis. *Nat. Methods*. 9:676–682. https://doi.org/10.1038/nmeth.2019

Schroeder, E.A., and G.S. Shadel. 2014. Crosstalk between mitochondrial stress signals regulates yeast chronological lifespan. *Mech. Ageing Dev.* 135:41–49. https://doi.org/10.1016/j.mad.2013.12.002

Shadel, G.S., and D.A. Clayton. 1997. Mitochondrial DNA maintenance in vertebrates. *Annu. Rev. Biochem.* 66:409–435. https://doi.org/10.1146/annurev.biochem.66.1.409

Shadel, G.S., and T.L. Horvath. 2015. Mitochondrial ROS signaling in organismal homeostasis. *Cell*. 163:560–569. https://doi.org/10.1016/j.cell.2015.10.001

Sheldon, L.A. 2017. Inhibition of E2F1 activity and cell cycle progression by arsenic via retinoblastoma protein. *Cell Cycle*. 16:2058–2072. https://doi.org/10.1080/15384101.2017.1338221

Shintaku, J., W.M. Pernice, W. Eyaid, J.B. Gc, Z.P. Brown, M. Juanola-Falgarona, J. Torres-Torronteras, E.W. Sommerville, D.M.E.I. Hellebrekers, E.L. Blakely, et al. 2022. RRM1 variants cause a mitochondrial DNA maintenance disorder via impaired de novo nucleotide synthesis. *J. Clin. Invest.* 132:e145660. https://doi.org/10.1172/JCI145660

Spelbrink, J.N., B.A. Van Oost, and C. Van den Bogert. 1994. The relationship between mitochondrial genotype and mitochondrial phenotype in lymphoblasts with a heteroplasmic mtDNA deletion. *Hum. Mol. Genet.* 3:1989–1997. https://doi.org/10.1093/hmg/3.11.1989

Suomalainen, A., and P. Isohanni. 2010. Mitochondrial DNA depletion syndromes--many genes, common mechanisms. *Neuromuscul. Disord.* 20:429–437. https://doi.org/10.1016/j.nmd.2010.03.017

Suomalainen, A., and J. Nunnari. 2024. Mitochondria at the crossroads of health and disease. *Cell*. 187:2601–2627. https://doi.org/10.1016/j.cell.2024.04.037

Taylor, S.D., H. Zhang, J.S. Eaton, M.S. Rodeheffer, M.A. Lebedeva, T.W. O'rourke, W. Siede, and G.S. Shadel. 2005. The conserved Mec1/Rad53 nuclear checkpoint pathway regulates mitochondrial DNA copy number in Saccharomyces cerevisiae. *Mol. Biol. Cell*. 16:3010–3018. https://doi.org/10.1091/mbc.e05-01-0053

Towers, C.G., B.E. Fitzwalter, D. Regan, A. Goodspeed, M.J. Morgan, C.-W. Liu, D.L. Gustafson, and A. Thorburn. 2019. Cancer cells upregulate NRF2 signaling to adapt to autophagy inhibition. *Dev. Cell*. 50:690–703.e6. https://doi.org/10.1016/j.devcel.2019.07.010

Tresse, E., J. Marturia-Navarro, W.Q.G. Sew, M. Cisquella-Serra, E. Jaberi, L. Riera-Ponsati, N. Fauerby, E. Hu, O. Kretz, S. Aznar, and S. Issazadeh-Navikas. 2023. Mitochondrial DNA damage triggers spread of Parkinson's disease-like pathology. *Mol. Psychiatry*. 28:4902–4914. https://doi.org/10.1038/s41380-023-02251-4

Ugi, S., T. Imamura, W. Ricketts, and J.M. Olefsky. 2002. Protein phosphatase 2A forms a molecular complex with Shc and regulates Shc tyrosine phosphorylation and downstream mitogenic signaling. *Mol. Cell. Biol.* 22:2375–2387. https://doi.org/10.1128/MCB.22.7.2375-2387.2002

Uhlik, M.T., B. Temple, S. Bencharit, A.J. Kimple, D.P. Siderovski, and G.L. Johnson. 2005. Structural and evolutionary division of phosphotyrosine binding (PTB) domains. *J. Mol. Biol.* 345:1–20. https://doi.org/10.1016/j.jmb.2004.10.038

West, A.P., W. Khoury-Hanold, M. Staron, M.C. Tal, C.M. Pineda, S.M. Lang, M. Bestwick, B.A. Duguay, N. Raimundo, D.A. MacDuff, et al. 2015. Mitochondrial DNA stress primes the antiviral innate immune response. *Nature*. 520:553–557. https://doi.org/10.1038/nature14156

Whitaker, R.M., D. Corum, C.C. Beeson, and R.G. Schnellmann. 2016. Mitochondrial biogenesis as a pharmacological target: A new approach to acute and chronic diseases. *Annu. Rev. Pharmacol. Toxicol.* 56:229–249. https://doi.org/10.1146/annurev-pharmtox-010715-103155

Wiley, C.D., M.C. Velarde, P. Lecot, S. Liu, E.A. Sarnoski, A. Freund, K. Shirakawa, H.W. Lim, S.S. Davis, A. Ramanathan, et al. 2016. Mitochondrial Dysfunction Induces Senescence with a Distinct Secretory Phenotype. *Cell Metab.* 23:303–314. https://doi.org/10.1016/j.cmet.2015.11.011

Woo, D.K., T.L. Phang, J.D. Trawick, and R.O. Poyton. 2009. Multiple pathways of mitochondrial-nuclear communication in yeast: Intergenomic signaling involves ABF1 and affects a different set of genes than retrograde regulation. *Biochim. Biophys. Acta*. 1789:135–145. https://doi.org/10.1016/j.bbagrm.2008.09.008

Wu, Z., S. Oeck, A.P. West, K.C. Mangalhara, A.G. Sainz, L.E. Newman, X.O. Zhang, L. Wu, Q. Yan, M. Bosenberg, et al. 2019. Mitochondrial DNA stress signalling protects the nuclear genome. *Nat. Metab.* 1:1209–1218. https://doi.org/10.1038/s42255-019-0150-8

Zeviani, M., C.T. Moraes, S. DiMauro, H. Nakase, E. Bonilla, E.A. Schon, and L.P. Rowland. 1988. Deletions of mitochondrial DNA in Kearns-Sayre syndrome. *Neurology*. 38:1339–1346. https://doi.org/10.1212/WNL.38.8.1339

Zhou, G., N. Jiang, W. Zhang, S. Guo, and G. Xin. 2021. Biomarker identification in membranous nephropathy using a long non-coding RNA-mediated competitive endogenous RNA network. *Interdiscip. Sci.* 13:615–623. https://doi.org/10.1007/s12539-021-00466-z

Supplemental material

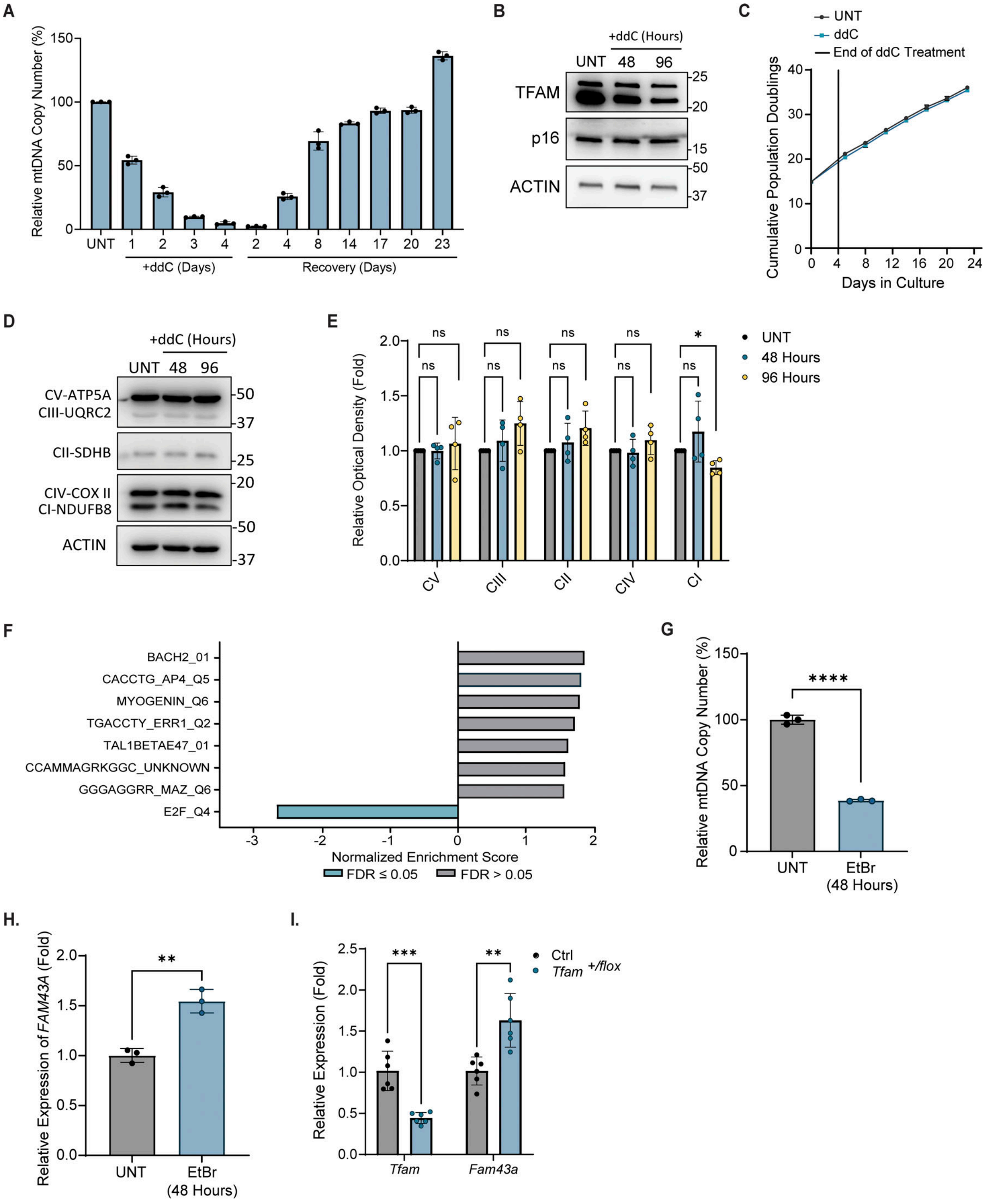

Figure S1. **Additional characterization of mtDNA-depleted IMR90 cells and expression of *FAM43A* in TFAM-depleted mouse liver tissue. (A)** IMR90 cells were treated with ddC (20 µM) for the indicated time. After 96 h of treatment, cells were cultured in a ddC-free medium for 23 days. The relative mtDNA copy number of untreated (UNT) and mtDNA-depleted and repleted cells was measured by qPCR. Data points represent the mean of three technical replicates from three biological replicates. Error bars represent mean ± SD. **(B)** Representative immunoblot image of TFAM (bottom band) and p16 in UNT and ddC-treated IMR90 cells. ACTIN was blotted as a loading control. **(C)** Cumulative population doublings of IMR90 cells treated as described in A. Data points represent the mean of three technical replicates from three biological replicates. **(D)** Representative immunoblots of OXPHOS subunits in UNT and ddC-treated IMR90 cells. **(E)** Quantification of (D) ($n = 4$ biological replicates). Error bars represent mean ± SD, Unpaired Student’s *t* test; ns, $P > 0.05$; *, $P < 0.05$. **(F)** Transcription factor motif analysis of differentially expressed genes in cells treated with ddC (20 µM) for 96 h. False discovery rate (FDR) and normalized enrichment score are shown. **(G)** Relative mtDNA copy number of untreated (UNT) and IMR90 cells treated with ethidium bromide (EtBr) (50 ng/ml) for the indicated time measured by qPCR using ND1 primers normalized to nuclear B2M ($n = 3$ technical triplicates). Error bars represent mean ± SD, Unpaired Student’s *t* test; ****, $P < 0.0001$. **(H)** Relative *FAM43A* mRNA level of UNT and IMR90 cells treated with EtBr for the indicated time measured by RT-qPCR normalized to *ACTIN* ($n = 3$ technical replicates). Error bars represent mean ± SD, Unpaired Student’s *t* test; **, $P < 0.01$. **(I)** Relative expression of *Fam43a* and *Tfam* in liver samples isolated from Ctrl (WT) and $\mathit{Tfam}^{+/flox}$ C57BL/6 mice ($n = 6$ mice per condition). Error bars represent mean ± SD, Unpaired Student’s *t* test; **, $P < 0.01$; ***, $P < 0.001$. Source data are available for this figure: SourceData FS1.

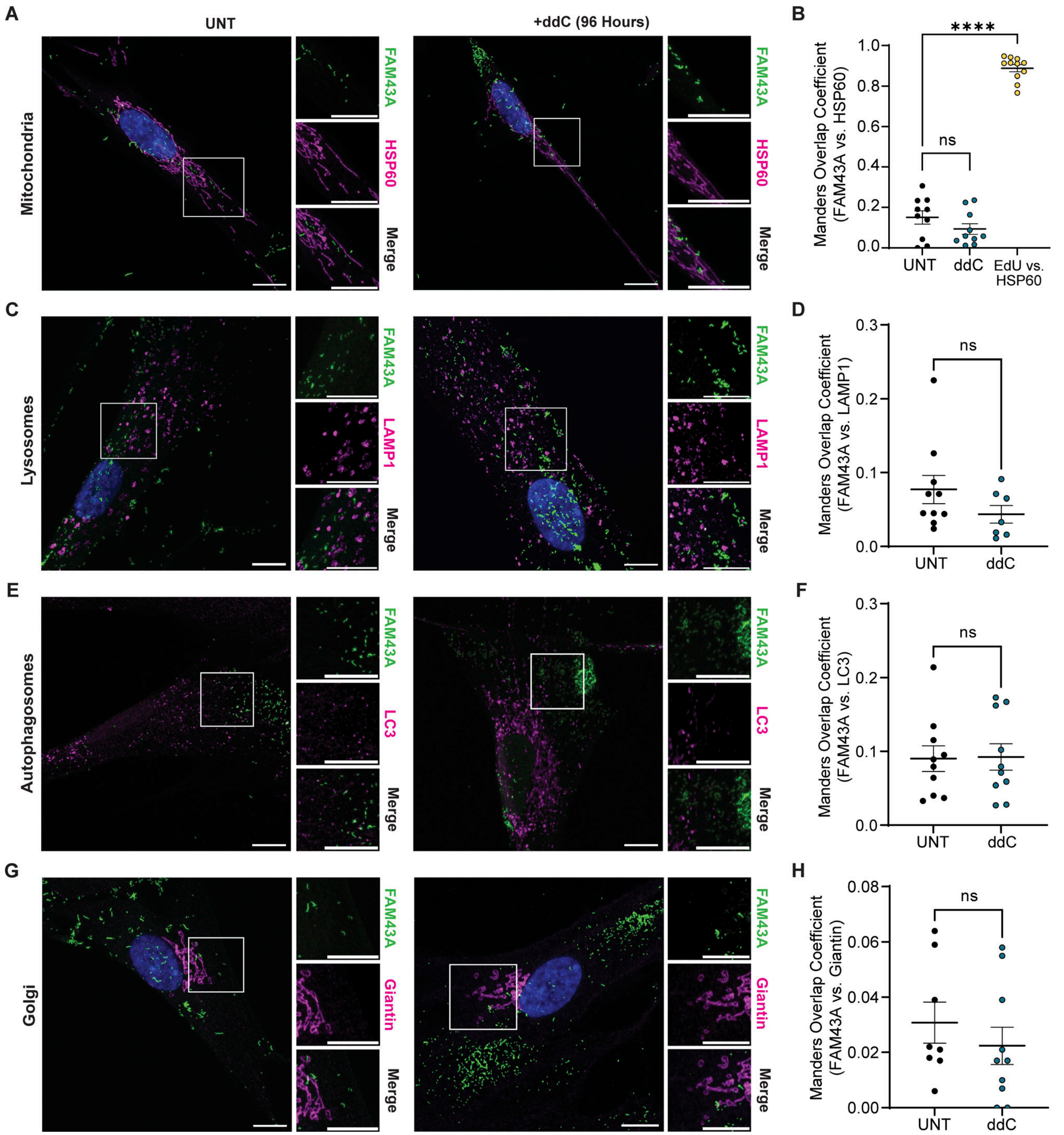

Figure S2. **FAM43A is a cytoplasmic protein under basal and mtDNA-depleted conditions. (A)** Representative Airyscan imaging of FAM43A (green) and HSP60 (mitochondria; magenta) in untreated (UNT) and ddC-treated IMR90 cells (20 µM; 96 h). **(B)** Quantification of Manders overlap coefficient of FAM43A vs. HSP60 and replicating mtDNA vs. HSP60 (positive control of colocalization). **(C)** Representative Airyscan imaging of FAM43A (green) and LAMP1 (lysosomes; magenta) in UNT and ddC-treated cells. **(D)** Quantification of Manders overlap coefficient of FAM43A vs. LAMP1. **(E)** Representative Airyscan imaging of FAM43A (green) and LC3 (autophagosomes: magenta) in UNT and ddC-treated cells. **(F)** Quantification of Manders overlap coefficient of FAM43A versus LC3. **(G)** Representative Airyscan imaging of FAM43A (green) and Giantin (Golgi: magenta) in UNT and ddC-treated cells. **(H)** Quantification of Manders overlap coefficient of FAM43A versus Giantin. In A, C, E, and G, the indicated regions are enlarged on the right with the merge of the two signals shown in the lower right corner. Cells were stained with Hoechst to visualize Nuclei (blue) where indicated. *n* = 7–11 cells/condition from two independent experiments. Scale bar: 10 µm. Error bars represent mean ± SEM, Unpaired Student's *t* test; ns, $P > 0.05$; ****, $P < 0.0001$.

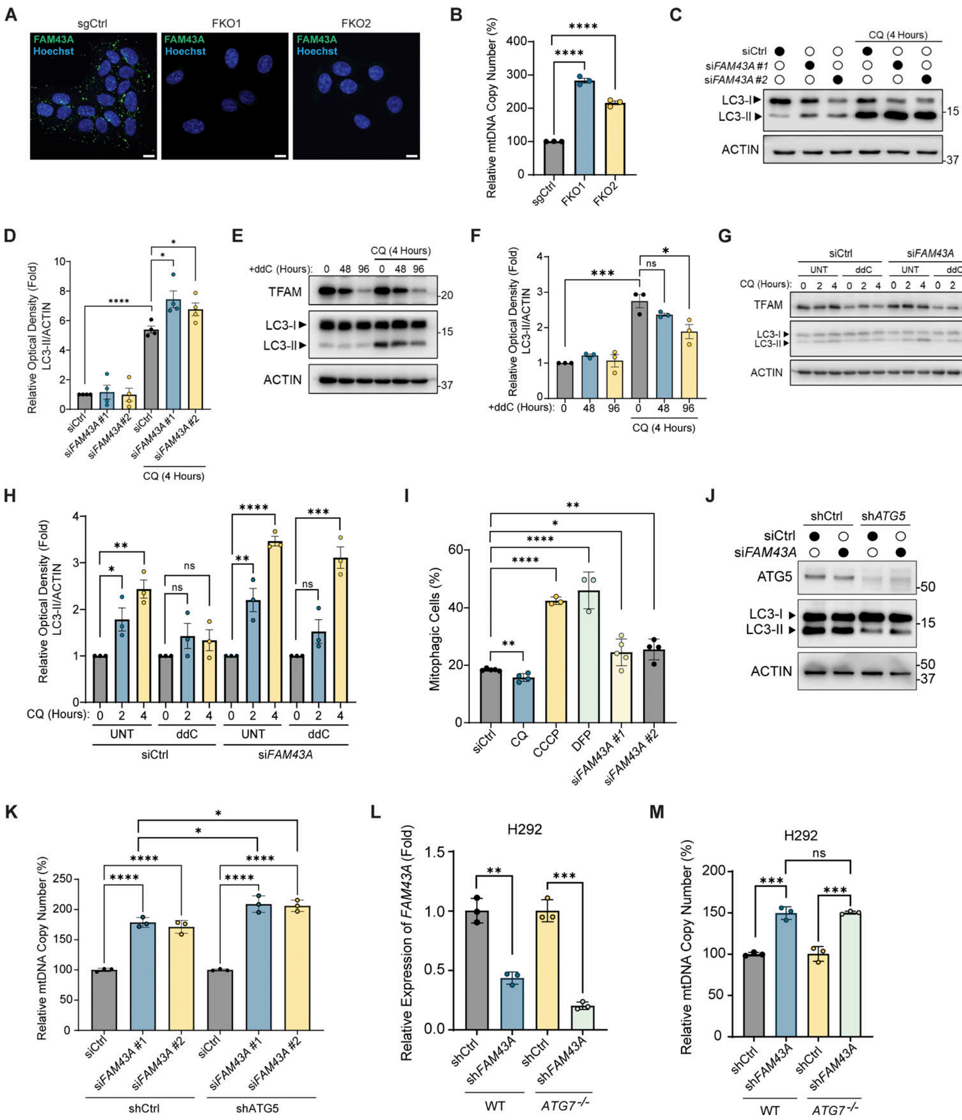

Figure S3. **Knockdown of *FAM43A* upregulates autophagy and mitophagy flux. (A)** Representative spinning disk imaging of FAM43A (green) and Hoechst (blue) in WT (sgCtrl) and *FAM43A* knockout (FKO) H292 cells verifying loss of FAM43A. Scale bar: 10 µm. **(B)** Relative mtDNA copy number of WT and FKO H292 cells measured by qPCR using ND1 primers normalized to nuclear B2M ($n = 3$ technical triplicates). Error bars represent mean ± SEM, Unpaired Student's *t* test; ****, $P < 0.0001$. **(C)** Representative immunoblots of LC3 and ACTIN (loading control) in IMR90 cells transfected with the indicated siRNA. 96 h after transfection, cells were treated with chloroquine (CQ) (50 µM) for 4 h. **(D)** Quantification of the ratio between the optical density (OD) of LC3-II and ACTIN from four independent experiments treated as in C. Error bars represent mean ± SD, multiple Unpaired Student's *t* test; *, $P < 0.05$. ****, $P < 0.0001$. **(E)** Representative immunoblots of TFAM, LC3, and ACTIN (loading control) of IMR90 cells treated with ddC (20 µM) for 48 or 96 h. Cells were treated with CQ 4 h prior to collection. **(F)** Quantification of the ratio between the optical density (OD) of LC3-II and ACTIN from three independent experiments treated as in E. Error bars represent mean ± SD, multiple Unpaired Student's *t* test; ns, $P > 0.05$; *, $P < 0.05$. ***, $P < 0.001$. **(G)** Representative immunoblots of TFAM, LC3, and ACTIN (loading control). IMR90 cells were transfected with either control (siCtrl) or siRNA against *FAM43A* (si*FAM43A* #1). Cells were treated with either vehicle (UNT) or ddC 48 h after transfection. Then, 96 h after transfection, cells were treated with CQ for the indicated time. **(H)** Quantification of the ratio between the optical density (OD) of LC3-II and ACTIN from three independent experiments treated as in G. Error bars represent mean ± SD, multiple Unpaired Student's *t* test; ns, $P > 0.05$; *, $P < 0.05$; **, $P < 0.01$; ****, $P > 0.0001$. **(I)** Quantification of mitophagy via ratiometric flow cytometry performed in IMR90 cells transfected with the indicated siRNA. After 72 h of transfection, siCtrl cells were treated with vehicle (UNT), CCCP (20 µM), Deferiprone (DFP 1 mM), or Chloroquine (CQ 50 µM) for 24 h before all samples were collected for flow cytometry. The data are shown as the ratio of PE-CF594/BV605 ($n = 3$–5 biological replicates/condition). Error bars represent mean ± SD, multiple Unpaired Student's *t* test; *, $P < 0.05$; **, $P < 0.01$; ****, $P < 0.0001$. **(J)** Representative immunoblots of ATG5, LC3, and ACTIN (loading control) in IMR90 cells stably expressing the indicated shRNA and transfected with the indicated siRNA for 96 h. **(K)** Relative mtDNA copy number of IMR90 cells stably expressing the indicated shRNA and transfected with the indicated siRNA for 96 h as measured by qPCR using ND1 primers and normalized to nuclear B2M. Data points represent the average of technical triplicates from three biological replicates. Error bars represent mean ± SD, one-way ANOVA with Dunnett's multiple comparisons; ****, $P < 0.0001$. **(L)** Relative *FAM43A* mRNA expression of wild-type (WT) and *ATG7* knockout H292 cells transfected with the indicated siRNA and collected 96 h after transfection. Data points represent the average of technical triplicates from three biological replicates. Error bars represent mean ± SD, multiple Unpaired Student's *t* test; **, $P < 0.01$: ***, $P < 0.001$. **(M)** Relative mtDNA copy number of WT and *ATG7* knockout H292 cells transfected with the indicated shRNA and collected 96 h after transfection as measured by qPCR using ND1 primers normalized to nuclear B2M ($n = 3$ technical replicates). Error bars represent mean ± SD, multiple Unpaired Student's *t* test; ns, $P > 0.05$: ***, $P < 0.001$. Source data are available for this figure: SourceData FS3.

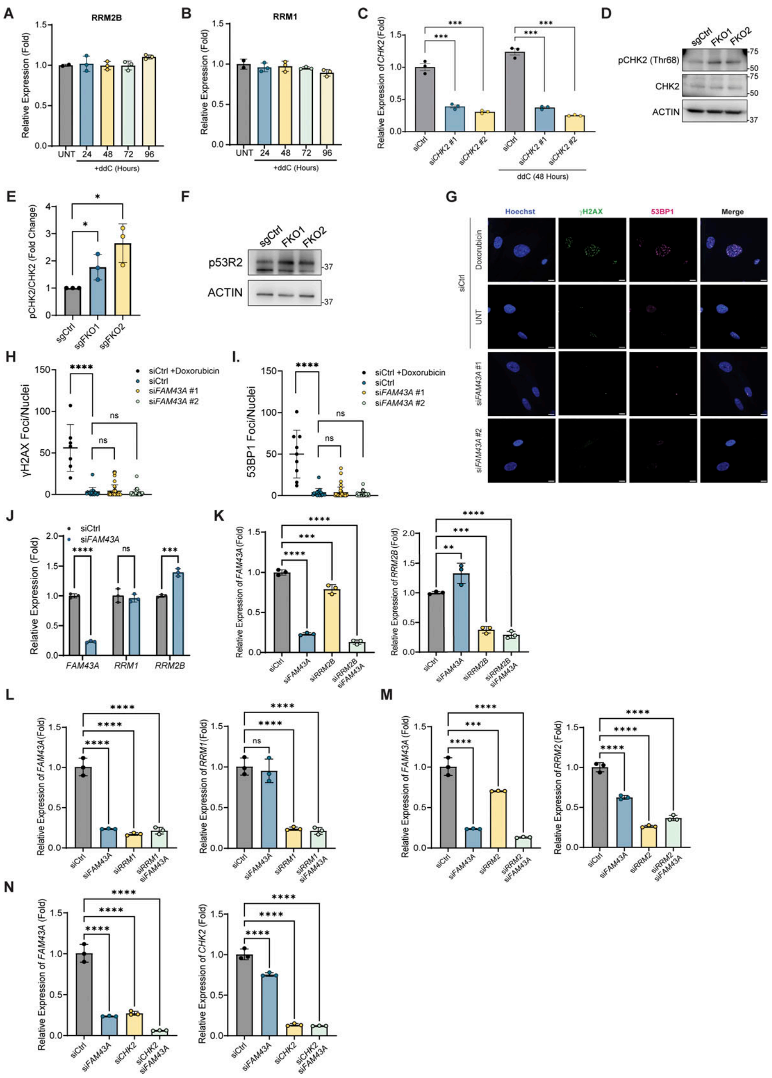

Figure S4. **Non-canonical CHK2 signaling activates RNR-dependent mtDNA synthesis in *FAM43A*-knockdown cells. (A and B)** Expression of *RRM2B* and (B) *RRM1* measured by RNA sequencing of IMR90 cells treated with ddC for the indicated time relative to untreated (UNT) control cells (n = 3 biological replicates). **(C)** IMR90 cells were transfected with the indicated siRNA. 96 h after transfection, cells were treated with ddC for 48 h. The relative mRNA expression of *CHK2* was measured by RT-qPCR normalized to *ACTIN* (n = 3 technical triplicates). Error bars represent mean ± SD, multiple Unpaired Student's *t* test; ***, P < 0.001. **(D)** Representative immunoblots of phosphorylated CHK2 (pCHK2 Thr68), CHK2, and ACTIN (loading control) in WT and *FAM43A* knockout (FKO) H292 cells. **(E)** Quantification of pCHK2 Thr68/CHK2 ratio from three independent experiments conducted as in D. The optical density of pCHK2 Thr68 and CHK2 were normalized to loading, and the ratio of pCHK2 Thr68 to total CHK2 was quantified as a measure of CHK2 activation. Error bars represent mean ± SD, multiple Unpaired Student's *t* test; *, P < 0.05. **(F)** Representative immunoblots of p53R2 (top band) and ACTIN (loading control) in WT and FKO H292 cells. **(G)** Representative Spinning disk imaging of Nuclei (Hoechst; blue), γH2AX (green), and 53BP1 (magenta) in cells transfected with the indicated siRNA for 96 h. Merge of the signals is shown in the right-hand column. Control (siCtrl) cells were treated with Doxorubicin (1 µM for 4 h) as a positive control for nuclear DNA damage. Scale bar: 10 µm. **(H and I)** Quantification of γH2AX and (I) 53BP1 foci/cell in G. Error bars represent mean ± SD, multiple Unpaired Student's *t* test; ns, P > 0.05; ****, P > 0.0001. n = 15–25 nuclei/condition. **(J)** Relative expression of *FAM43A*, *RRM1*, and *RRM2B* in cells transfected with the indicated siRNA (siCtrl and si*FAM43A* #1) and collected 96 h after transfection (n = 3 technical triplicates). Expression was measured by RT-qPCR and normalized to *ACTIN*. Error bars represent mean ± SD, multiple Unpaired Student's *t* test; ns, P > 0.05; ***, P < 0.001; ****, P < 0.0001. **(K)** Relative expression of *FAM43A* and *RRM2B* normalized to *ACTIN* as measured by RT-qPCR. Cells were transfected with control or siRNA against RRM2B. 48 h after transfection, cells were transfected with siRNA against FAM43A and collected 96 h later. Data points represent the average of technical triplicates from three biological replicates. Error bars represent mean ± SD, one-way ANOVA with Dunnett's multiple comparisons; **, P < 0.01; ***, P < 0.001; ****, P < 0.0001. **(L)** Relative expression of *FAM43A* and *RRM1* in cells transfected with the indicated siRNA as in K. Expression was measured by RT-qPCR and normalized to *ACTIN*. Data points represent the average of technical triplicates from three biological replicates. Error bars represent mean ± SD, one-way ANOVA with Dunnett's multiple comparisons; ns, P > 0.05; ****, P < 0.0001. **(M)** Relative expression of *FAM43A* and *RRM2* of cells transfected with the indicated siRNA as in K. Expression was measured by RT-qPCR and normalized to *ACTIN*. Data points represent the average of technical triplicates from three biological replicates. Error bars represent mean ± SD, one-way ANOVA with Dunnett's multiple comparisons; ***, P < 0.001; ****, P < 0.0001. **(N)** Relative expression of *FAM43A* and *CHK2* of cells transfected with the indicated siRNA as in K. Expression was measured by RT-qPCR and normalized to *ACTIN*. Data points represent the average of technical triplicates from three biological replicates. Error bars represent mean ± SD, one-way ANOVA with Dunnett's multiple comparisons; ****, P < 0.0001. The expression of *FAM43A* was normalized to the same control (siCtrl) sample in panels L–N. Source data are available for this figure: SourceData FS4.

Provided online are Table S1, Table S2, and Table S3. Table S1 shows normalized raw counts from RNA-seq analysis of IMR90 cells treated with vehicle (water) or ddC for 24, 48, 72, or 96 h. Table S2 shows results of differential gene expression analysis of RNA-seq of IMR90 cells treated with ddC. Table S3 shows enriched transcription factor networks in IMR90 cells treated with ddC for 96 h.